D4.6. Final WP4 scientific report

WP4 – End user of Energy and prosumers

Author: NOVA University Lisbon (UNL)

March 2026

SMARTGYSUM project has been funded by the European Commission's Horizon 2020 Programme

SMARTGYSUM project has been funded by the European Commission's Horizon 2020 Programme

SMARTGYsum has been funded by the European Union's Horizon 2020 Programme under the Grant Agreement GA 955614

Versions:

Version No.	Person in charge	Institution (acronym)	Date	Comments
1	Oleksandr Velihorskyi	CNUT	18.06.2023	First template of the deliverable report
2	João Martins	UNL	25.03.2026	First draft
3	Oleksandr Velihorskyi	CNUT	30.03.2026	General Checking
4	Enrique Romero	UEX	30.03.2026	Approval and PDF creation for uploading

SMARTGYSUM project has been funded by the European Commission's Horizon 2020 Programme

Technical References:

Project Acronym	**SmartGYsum**
Project Title	Research and Training Network for Smart and Green Energy Systems and Business Models
Project Coordinator (PC)	Enrique Romero (eromero@unex.es) Universidad de Extremadura (UEX)
Project Duration	1 October 2021 – 31 March 2026

Deliverable No.	D4.6
Dissemination Level	Public
Work Package	WP4 – End user of Energy and prosumers
Tasks	
Lead Beneficiary	14 – UNL
Contributing beneficiary (ies)	CYP, TUT, USA
Data due of deliverable	---
Actual submission date	---

Table of Contents

List of abbreviations

AFE	Active Front End
BEN	Beneficiary
BESS	Battery Energy Storage System
BRIG	BRIGHTLOOP CONVERTERS (Company)
CYP	CY Cergy Paris Université (Partner)
Dn	Deliverable (number)
DoA	Description of Action
DS	Doctoral School
EOL	End of Life
EMS	Energy Management System
ER	Energy Router
ESR	Early-Stage Researcher
ESS	Energy Storage System
ETN	European Training Network
GA	Grant Agreement
IRP	Individual Research Project
ICT	Information and Communication Technologies
ITN	Innovative Training Network
MSn	Milestone (number)
NILM	Non-Intrusive Load Monitoring
KIT	KARLSRUHER INSTITUT FUER TECHNOLOGIE (Partner)
MSCA	Marie Sklodowska-Curie Actions
OPAL	OPAL RT Technologies (Company)
PC	Project Coordinator
PV	Photovoltaic
REC	Research Ethics Committee
RSC	Recruitment and Secondment Committee
SOC	State of Charge
SoH	State of Health
ToU	Time of Use (tariff)
UNL	UNIVERSIDADE NOVA DE LISBOA (Partner)
USA	UNIVERSITA DEGLI STUDI DI SALERNO (Partner)
WPn	Work Package (number)

SMARTGYSUM project has been funded by the European Commission's Horizon 2020 Programme

1. Executive summary

This final scientific report for Work Package 4 outlines the extensive progress and technical outcomes achieved in the "End user of Energy and prosumers" domain. The overarching objectives of this work package centered on identifying novel strategies for electric energy use and energy storage systems, reducing overall consumption through the implementation of smart metering technologies, and analyzing the cooperation between power converters and Information and Communication Technologies within Energy Management Systems. Additionally, the project aimed to pinpoint the behavioral changes necessary to actively engage customers in modern energy applications. To systematically address these goals, the research was structured into three Individual Research Projects conducted by Early Stage Researchers.

The first primary research area focused on creating an edge computing platform tailored for fault-tolerant, highly reliable, and resilient power electronics in prosumer applications. A cornerstone of this task was the development of a bottom-up residential load profile generator. Rather than relying on historical smart meter data, this innovative tool reconstructs a household's total electricity demand by combining appliance-level models – such as water heaters, heat pumps, and washing machines – with real-time weather conditions and occupancy schedules. In tandem, the researchers established a comprehensive modeling framework for photovoltaic and battery systems that incorporates battery lifetime estimation and degradation-aware cost assessments. These advanced models were used to drive day-ahead energy management optimization, striking a balance between investment and operational costs. To validate the practical applicability of these theoretical models, the residential load generator was successfully deployed on a low-cost Raspberry Pi 4 integrated seamlessly with the Home Assistant platform.

The second research initiative shifted the focus toward designing robust Energy Management Systems for residential microgrids that feature integrated energy storage. The research successfully demonstrated the efficacy of a centralized management system that leverages the communication protocols to orchestrate microgrid operations. This centralized approach enabled critical systemic functions, including precise power balancing and State of Charge balancing among various connected converters. Furthermore, the team showcased a price-based Energy Management System that uses droop curve shifting as a primary control mechanism, dynamically modifying the droop parameters of the battery interface converter in direct response to fluctuating electricity prices. Key practical achievements within this task also included the deployment of an online monitoring and logging platform for direct current microgrids, alongside a Controller Hardware in the Loop implementation designed to rigorously test diverse energy management scenarios.

The final research segment advanced both demand-side and supply-side intelligence for smart buildings, heavily based on a decentralized, edge-based architectural approach. On the demand side, a highly robust Non-Intrusive Load Monitoring framework was developed to disaggregate appliance-level loads from a single aggregated active-power signal. This framework stands out for its resilience against unknown loads and domain shifts, using a probabilistic state update mechanism that bypasses the need for constant retraining. On the supply side, the researchers proposed an adaptive Double Single-Diode Model for photovoltaic parameter identification. By separating solar cells into distinct irradiance groups, this self-adapting formulation maintains physical consistency even under partial shading or mismatch conditions, allowing for the accurate tracking of degradation effects directly from current-voltage curves. Both the load monitoring and photovoltaic diagnostic tools were unified as software add-ons and executed concurrently in real-time on a Raspberry Pi-based platform.

Ultimately, the final report for Work Package 4 illustrates substantial scientific and practical progress in the localized control, interpretability, and monitoring of prosumer energy systems. By successfully shifting complex computational requirements and diagnostic frameworks away from the cloud and onto low-cost edge computing platforms, the SMARTGYSUM project has delivered practical, deployable technologies that pave the way for the modernization and resilience of residential microgrids and smart buildings.

1.1. Objectives of the deliverable

The objective of the final scientific report is to compile the results obtained in the corresponding IRPs included in the WP4.

1.2. Organisation of the deliverable

This deliverable is organized into six main sections to provide a comprehensive overview of the progress and outcomes of Work Package 4. Section 1 introduces the document, presenting an executive summary alongside the primary objectives and organization of the report. Section 2 details the general progress of the action, which includes a review of the overarching WP4 objectives, the specific tasks involved, and a summary of the individual researchers' statuses and general evaluations. Section 3 forms the core scientific body of the deliverable, providing an in-depth breakdown of the progress across the three main tasks: Task 4.1 (IRP9) focusing on edge computing platforms for power electronics, Task 4.2 (IRP10) covering energy management systems for residential micro-grids, and Task 4.3 (IRP11) detailing the online diagnosis and optimization frameworks for smart buildings. For each of these tasks, the section elaborates on the introduction, specific scientific outcomes, contributions to the wider work package objectives, and notable scientific achievements such as publications and prototypes. Finally, the report is rounded out by Section 4, which provides the overall conclusions, followed by Section 5 for the references and Section 6 containing the supplementary annexes.

2. General progress of the action

2.1. WP4 Objectives and tasks

WP4 (End user of Energy and prosumers) objectives are:

i. to identify and demonstrate new ways of using electric energy enabling ESS and consumption strategies using monitoring and exogenous information;
ii. to reduce energy consumption by using emergent technology as smart meters
iii. to analyse the benefits and possibilities of cooperation between power converters and ICT in Energy Management Systems;
iv. to identify the main energy-related behaviour change requirements necessary to engage customers in energy applications.

WP4 (End user of Energy and prosumers) tasks are:

- Task 4.1: Development of embedded real-time system to enhance the tolerance and reliability of power electronics (UNL-USA-BRIG).
- Task 4.2: Design and in-loop Residential Energy Management Systems based on microgrid integrated Energy Storage Systems (UNL-KIT-OPAL).
- Task 4.3: On-line diagnosis and optimization of Energy Management Systems for Smart Buildings (UNL-USA).
- Task 4.4: Elaboration of partial and final scientific reports (UNL)

2.2. WP4 – Workpackage progress

(Include here a summary about when each IRP started that is supposed to be the recruitment date of the ESR. Please indicate if ESR there were two ESR's in the same position in different time – in such a case please add additional row for specified ESR)

ESR	Starting date / end date	General evaluation	Status
9	May 2023/May 2026	The objectives set to the ESR were achieved in terms of publications, secondments, participation to the doctoral schools. The scientific contributions of his work are satisfactory as well: development of a generic load profile application, multiparametric optimization of a day-ahead schedule to be implemented in an EMS for a residential household.	In progress. The thesis will be defended on time.
10	01/02/2023-31/05/2023	The first ESR worked on grid interface (AFE) converter within the work period and developed core functionalities and advanced modulation techniques for the AFE converters. The ESR's work results have been presented in 8 IEEE conference papers, 5 workshops & symposiums, 1 book chapter and 1 journal paper. The activities have been interrupted in June 2023 in accordance with the request of the employee.	Finished
10	01.11.2023 - 30/06/2025	The second ESR started from 01 Nov 2023. He worked on energy management system part of the IRP10. He has published 6 conference papers, 2 journal articles, and 1 book chapter, and attended several doctoral schools and training courses. He is currently a 3rd-year doctoral student at TalTech.	Finished
11	01/11/2022	The major accomplishments achieved in the project are summarized below: -Integrated architecture for decentralized smart-building monitoring. The project defined and validated an edge-based architecture where a single embedded device performs both appliance-level load disaggregation and PV diagnostic parameter estimation, processes data locally, and exposes results through a unified interface to support EMS actions (e.g., anomaly	Completed

		detection, improved self-consumption strategies, and informed scheduling of controllable loads). -Demand-side contribution: robust NILM analysis and a training-less NILM method for edge devices. The project quantified how domain shifts (notably unknown appliances) degrade the performance of convolutional neural network NILM models, providing a theoretical and experimental basis for improved robustness. It then proposed a lightweight training-less NILM framework that tracks appliance operation through probabilistic state modeling and efficient sequential inference, achieving strong robustness and computational efficiency on public datasets. -Supply-side contribution: PV parameter identification for reliable diagnostics using only I–V curves. The project developed a self-adapting PV modeling approach designed to remain stable under both uniform and mismatched conditions. A robust fitting strategy and evolutionary estimation enable accurate parameter extraction directly from I–V curves, with demonstrated capability to track degradation effects (e.g., series resistance increases) and improved practicality compared to methods requiring additional specialized measurements. -Unified implementation and validation on low-cost embedded hardware, plus a deployment pathway. The NILM and PV diagnostic methods were implemented as add-ons running concurrently on a Raspberry Pi–based platform integrated with Home Assistant, demonstrating real-time operation without overloading the device. A commercialization framework was also proposed to support scalable adoption via a hybrid edge–cloud service model while preserving privacy and low-latency performance. The PhD thesis has been successfully defended, and a double title degree has been jointly awarded from the Cergy Paris University and the University of Salerno.	

3. WP4 Tasks progress

3.1. Task 4.1 – IRP9 "Edge Computing Platform for Fault Tolerant, High Reliable and Resilient Power Electronic in Prosumers Applications"

3.1.1. Introduction

Task 4.1 addresses the development of methods and tools for prosumer energy systems. In this context, the work carried out focused on the modelling and optimization of residential energy systems integrating controllable loads, photovoltaic generation, and battery energy storage.

The research activities covered several complementary aspects. First, a residential load profile generator was developed to provide short-term demand prediction based on appliance-level modelling, weather conditions, and occupancy schedules. Second, a detailed PV–battery system modelling framework was established, including battery lifetime estimation and degradation-aware cost assessment. These models were then used to support day-ahead energy management optimization.

Overall, the work provides a basis for the development of Home Energy Management Systems suitable for residential prosumer applications, while also supporting future deployment on low-cost embedded and edge-computing platforms.

3.1.2. Scientific outcomes

This work developed a residential load profile generator for Home EMS. The proposed approach reconstructs the total household electricity demand from appliance-level models rather than relying on historical smart meter data. It integrates the thermal and operational behaviour of major household appliances, including the water heater, heat pump, refrigerator, and washing machine, while also accounting for occupancy schedules and weather-related variables such as outdoor temperature, inlet water temperature, and solar irradiance.

The main contribution lies in providing a framework able to generate realistic 24-hour household load profiles under different seasonal and occupancy conditions. The results showed that the model captures both variations in total daily consumption and changes in load shape, with weather conditions mainly affecting energy demand and occupancy influencing peak periods and appliance usage.

To demonstrate practical applicability, the complete load generator was implemented on a Raspberry Pi 4 and integrated into Home Assistant. This confirmed that the proposed method is compatible with low-cost embedded platforms and can be used as a forecasting layer for future residential energy management and optimization applications.

3.1.3. Appliance Load Modelling

A bottom-up modelling approach was adopted to represent residential electricity consumption. The total household load is reconstructed from the behaviour of key appliances, including thermostatically controlled devices and common household equipment. Each appliance is modelled using simplified physical or operational representations that capture its main dynamics.

Water Heater (WH)

A comprehensive model of the water heater system is depicted in Figure 1.1. Based on it, a hot water consumption profile is first created. It depends on the number of occupants and their age. The average daily hot water requirement is 56 liters per adult at 40°C. The volume of the water heater can be determined based on the average consumption of each occupant, as illustrated in (1.1).

$$\mathrm{V} = \mathrm{N}_p V_i. \tag{1.1}$$

Where *Np* represents the number of occupants in the house, and V_i represents the average volume of water consumed per day. In this paper it is chosen equal to 50 litters.

The temperature evolution within the tank is described by (1.2).

$$C_{wh}\frac{dT_T(t)}{dt} = W_d(t)\rho C_p\left(T_{in} - T_T(t)\right) + A_{wh}\left(T_a - T_T(t)\right) + Q_{WH}. \quad (1.2)$$

Where T_T(°C) is the temperature of water in the tank, T_{in}(°C) is the inlet water temperature, T_a(°C) is the ambient temperature, $\rho(Kg/m^3)$ represents the water density$C_p(\mathrm{J}/Kg°C)$ is the specific heat of water, $V(m^3)$: Volume of water tank and C_{wh}(J/°C) represents thermal capacity of water in the tank, $C_{wh} = \rho C_p V$.

A_{wh}(W/°C) is the thermal conductance of the tank, Q_{WH}(W) is the electric power input, P_N (W) is the nominal power of the water heater, and $W_d(m^3/\mathrm{s})$ represents the hot water consumption.

It shall be noted that the ambient temperature variation is considered yet its impact is not significant since usually the hot water tank is isolated. The most influencing factor in this equation is the temperature of the cold inlet water. It is worth noting that the water provider companies in France monitor the water temperature at the plant to maintain it typically around 12°C. However, this temperature can fluctuate at the consumer's location between 10°C and 25°C, this variation could be due to heat exchange with external temperature pipelines or other factors.

W_d is the hot water flow rate from the tank. It is computed using (1.3).

$$W_d(t) = W_{user}(t)\frac{T - T_{in}}{T_T - T_{in}}. \quad (1.3)$$

The hot water at temperature T_T is mixed with cold water at temperature T_{in} to supply users with the desired temperature T (40°C) at the rate W_{user}. It is important to note that the hot water draw durations are very short.

Low-tariff period is applied (as it is commonly the case in France): this means that the water inside the tank is heated up during the night (low tariff) in order to provide the predicted hot water, need during the next day. The temperature inside the water heater is regulated to remain within a predefined range as summarized in Table 1.1.

The Q_{WH} is computed accordingly as in (1.4).

$$W_d(t) = W_{user}(t)\frac{T - T_{in}}{T_T - T_{in}}. \quad (1.4)$$

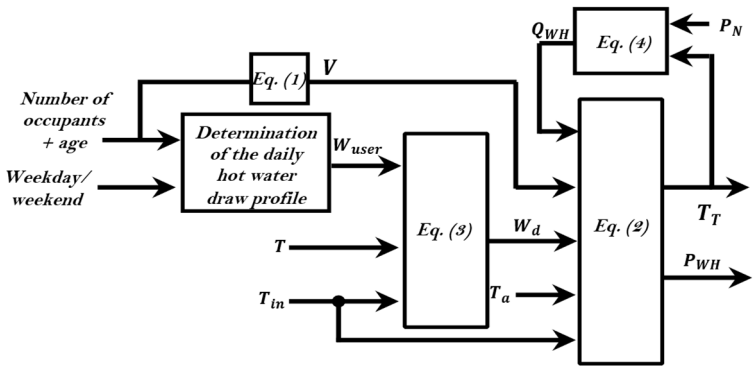

Fig. 1.1. Three-phase HFLC topology

Table 1.1: Temperature settings based on electricity tariff

During the low tariff		During the high tariff	
$T_{WH_{min}}$	$T_{WH_{max}}$	$T_{WH_{min}}$	$T_{WH_{max}}$
55°C	60°C	40°C	45°C

The user's hot water consumption profile represents a total water consumption of 193 litters at 40°C with a flow rate of 7 liters per minute. Figure 1.2 illustrates the electrical power consumption profile for the water heater on weekday

in August, the inlet water temperature fluctuated between 16°C and 22°C. The effect of the inlet water temperature is significant, causing a decrease in the temperature inside the tank. The water heater operates during the evening hours, coinciding with peak electricity tariffs due to the high demand for hot water. Additionally, the influence of ambient temperature was also observed, resulting in a slight decrease in the temperature inside the tank.

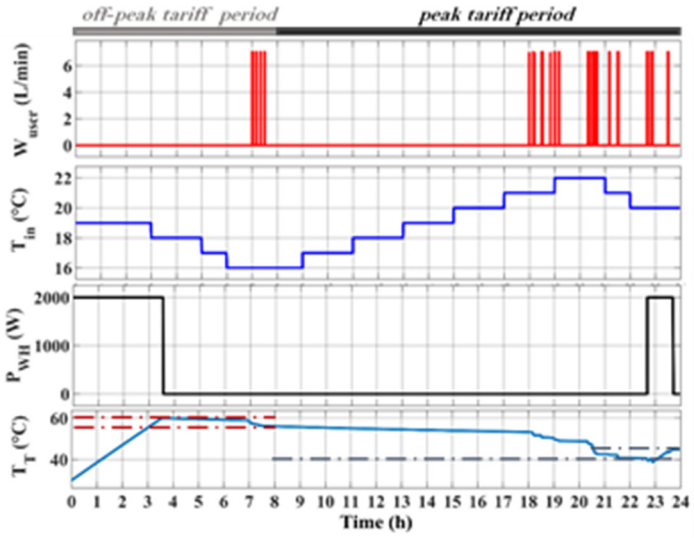

Fig. 1.2. 24-hour power consumption profile and temperature evolution for Water Heater.

Cooling/heating system

The Heat Pump (HP) use for heating/cooling increased in recent years especially in France, in line with the goals set by the government for replacing coal or oil-fired heaters. There are several types of heat pumps. The reversible air/air heat pump is a widely adopted technology in the European market and is by consequence the one retained for this study.

The temperature evolution within the house is described in (1.5), which serves as ambient temperature inputs for the refrigerator and water heater.

$$C_i \frac{dT_i(t)}{dt} = G_{eq}\left(T_{out} - T_i(t)\right) + \emptyset_{pr} + Q_{HP}(t) \quad (1.5)$$

Where $T_i(°C)$ is the indoor temperature,$T_{out}(°C)$ is the Outdoor temperature, $V_h\ (m^3)$ is the volume of the house, $\rho_0(kg/m^3)$ is the air density, $C_0(J/kg°C)$ is the specific heat of air and $C_i\ (J/°C)$ represents the thermal capacity of air in the house, $C_i = \rho_0 C_0 V_h$.

$\emptyset_{pr}(W)$ is the heat generated by cooking appliances, which is considered by adding some heat to the house while these appliances are in use and $Q_{HP}(W)$represents the thermal power produced by the heat pump.

The calculation is done under the assumption of a uniform temperature within the house without considering partitions. Such simplification of the mathematical model doesn't lead to the significant degradation of the estimation of power consumption. Figure 3 presents a proposed model for the heating/cooling system.

$G_{eq}(W/°C)$ is the equivalent thermal transmittance of the house. It is the sum of the wall, roof and windows transmittance weighted by their respective surfaces as computed in (1.6).

$$G_{eq} = G_{\mathrm{W}} + G_{\mathrm{wi}} + G_r = \vartheta_W S_W + \vartheta_r S_r + \vartheta_{wi} S_{wi} \quad (1.6)$$

Where $\vartheta_i(W/\mathrm{m}^2.°C)$ represents the thermal transmittance per square meter of the considered material. In the studied case, the isolation of the house complies with RT2012 and the values of the ϑ_i are chosen accordingly.

The heating/cooling system is programmed to maintain the indoor temperature within specific ranges depending on the season and the occupancy as summarized in Table 1.2.

Table 1.2: Indoor temperature settings based on occupancy

	Winter			Summer	
	$T_{h_{min}}$	$T_{h_{max}}$	Overnight $T_{h_{min}}$	$T_{c_{min}}$	$T_{c_{max}}$
Occupancy	19°C	21°C	17°C	25°C	26°C
No occupancy	16°C	17°C	16°C	HP OFF	HP OFF

Q_{HP} is computed by depending on the season as shown in (7) and (8).

In winter:

$$Q_{HP}(t) = \begin{cases} KQ_{HP_{max}}(T_{set} - T_i) & if\ T_i \leq T_{h_{min}} \\ 0 & if\ T_i \geq T_{h_{max}} \end{cases} \quad (1.7)$$

$$Q_{HP}(t) = \begin{cases} -KQ_{HP_{max}}(T_{set} - T_i) & if\ T_i \geq T_{c_{min}} \\ 0 & if\ T_i \leq T_{c_{max}} \end{cases} \quad (1.8)$$

Where: K is the proportional gain, $Q_{HP_{max}}(W)$ is the maximum thermal power of the heat pump and $T_{set}(°C)$ is the indoor air set-point temperature. The electric power consumption by the heat pump, denoted as Pe(t), is determined by dividing Q_{HP} by the efficiency factor γ as illustrated in Figure 1.3.

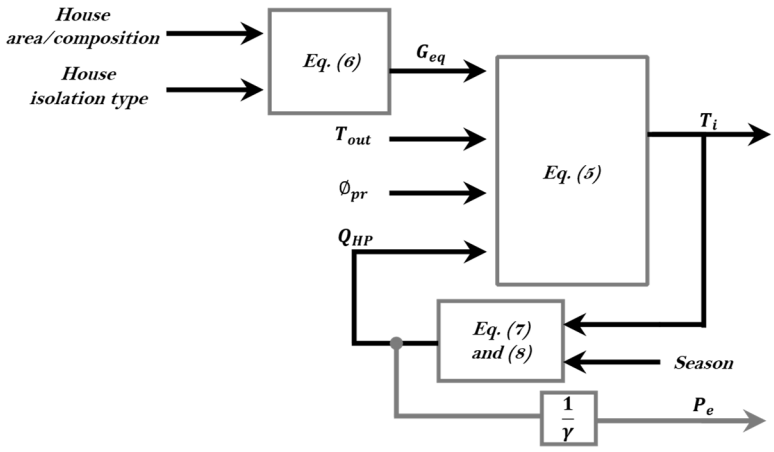

Fig. 1.3. Heat pump model.

Figure 1.4 illustrates the variation of indoor temperature and demonstrates the heat pump response to maintain this temperature within an acceptable range, considering the presence of residents in the house and the program settings presented in Table 2 during winter temperatures.

Refrigerator

In France, refrigerators consume approximately 166 to 450 kWh/year. This higher energy consumption is attributed to their continuous 24-hour operation. Their energy consumption depends on the state of the compressor (ON/OFF) that is controlled by a thermostat. The ambient temperature is recognized as the most influential parameter affecting the energy consumption of domestic refrigerators.

The temperature evolution within the refrigerator is described in (1.9).

$$C_r \frac{dT_r(t)}{dt} = \frac{1}{R_r}\left(T_a - T_r(t)\right) - P_R(t) \quad (1.9)$$

Where $T_r(°C)$ is refrigerator's indoor temperature, $C_r(J/°C)$ the thermal mass of refrigerator, $R_r(°C/W)$ is the thermal resistance of the refrigerator's envelope, $P_{R_r}(W)$ is the refrigerator's nominal power.

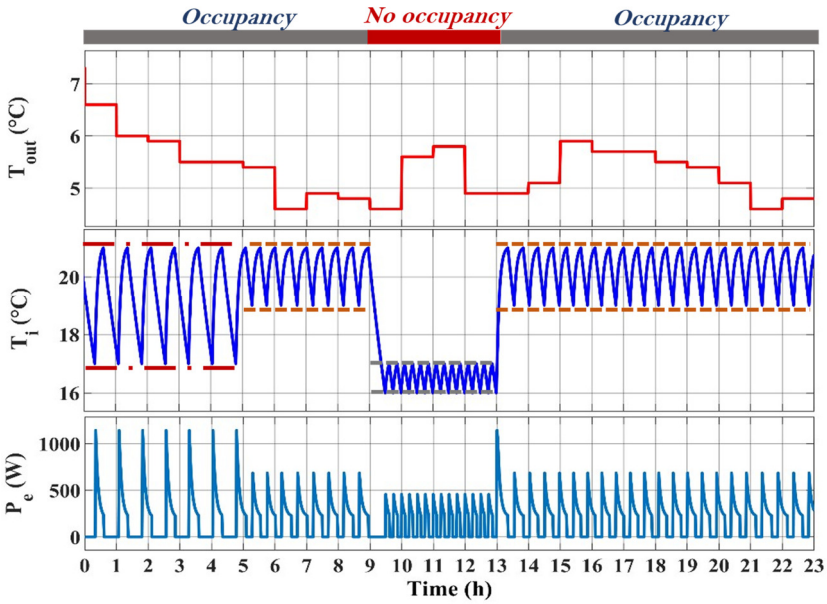

Fig. 1.4. Heat Pump load profile for winter time.

$P_R(t)$: Electric power input (W), and its expression is given by (1.10).

$$P_R(t) = \begin{cases} P_{R_n} & if\ T_r \geq T_{r_{max}} \\ 0 & if\ \ T_r \leq T_{r_{min}} \end{cases} \quad (1.10)$$

Figure 1.5 shows the impact of the ambient temperature on the ON duration of the compressor in addition to the number of cycles for a same period of time. These results justify the importance of considering this parameter, which, in this case, is the heat pump output temperature T_i.

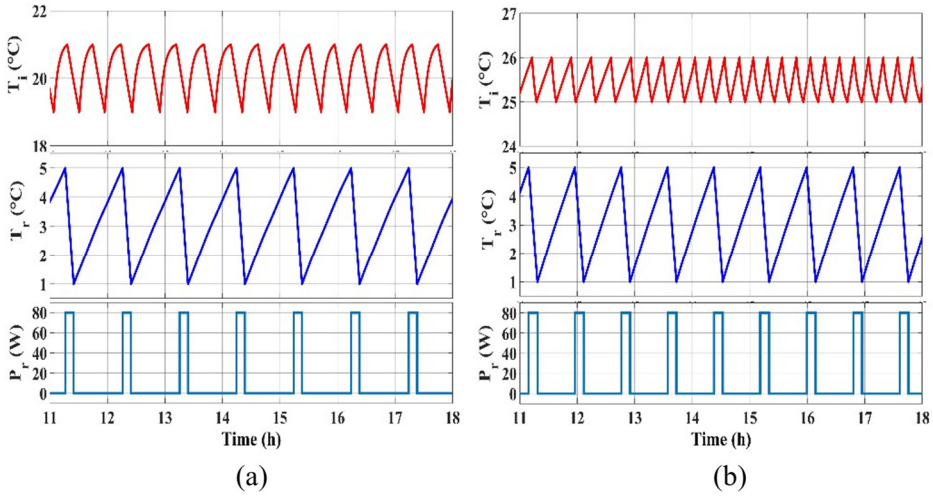

Fig. 1.5. Refrigerator Power Consumption Profile: (a) for winter time, (b) for summer time.

Washing machine

A study that pretends to include all the possible available wash programs is practically unfeasible. Therefore, only the most commonly used ones are considered: synthetic wash cycles. Regardless of the cycle, a washing machine operation consists of three uninterruptible phases: water heating, washing, and spinning. When the latter two have almost constant consumption (an average of 80W and 150W respectively), more attention is paid to the first phase since its duration and consequently consumption depend on the selected temperature for the laundry in addition to the inlet cold water temperature.

A thermal model for the water heating phase is proposed in (1.11).

$$T_{WM}(t) = \frac{P_{Heating}}{C_{wm}} t + T_{in} \quad (1.11)$$

Where $T_{WM}(°C)$ is the water temperature inside the washing machine drum, $P_{Heating}(W)$ is the electric power of heating cycle, $V_{wm}(m^3)$ is the volume of water for the washing cycle, $C_{wm}(\mathrm{J/°C})$ is the thermal capacity of water in the drum, $C_{wm} = \rho C_p V_{wm}$.

The impact of the inlet cold water on the cycle duration is proven in Figure 1.6. This difference in the duration of washing cycles illustrate the impact of temperature on energy consumption, as it results in a longer water heating duration.

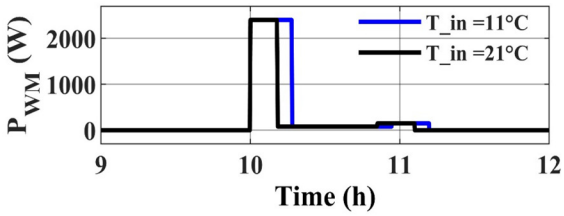

Fig. 1.6. Washing machine power profile at different inlet cold water temperatures.

Washing machine

Figure 1.7 presents a comprehensive generic load profile model depicting main blocks that include appliances models and program inputs. The appliance control block concerns the part of the program dedicated to controllable residential loads, such as water heater and heat pump.

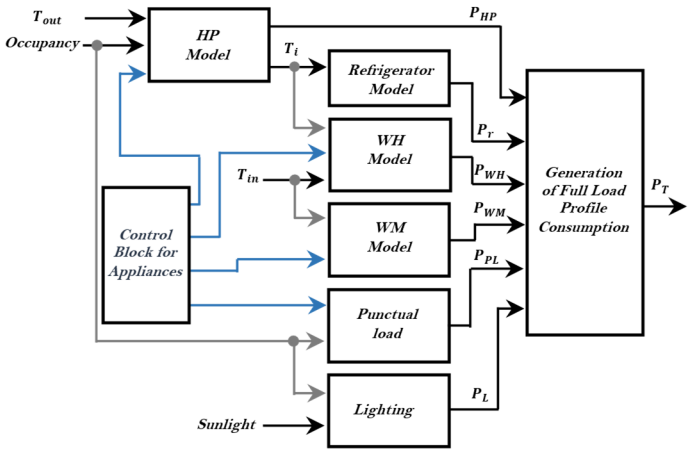

Fig. 1.7. Generic load profile model.

This generic model makes it possible to manage appliances as part of EMS, which can reduce energy consumption prices and demand peaks. Many simulations were conducted to validate the complete model and to provide a deeper insight into how weather data inputs and occupancy impact energy consumption.

Figures 1.8(a) and 1.8(b) show the occupancy profiles, indoor and outdoor temperatures, and solar irradiance to observe their impact on the load profile in summer and winter. The difference is evident when comparing the two figures, especially for thermostatically controlled appliances where temperature plays a significant role in their operation. The heat pump operates in both cooling and heating modes to meet occupants' comfort requirements. The sunlight significantly influences lighting load, especially on prolonged sunny days, while the impact of occupancy is notably evident between Figures 8(a) and 8(b), specifically for punctual load and ON/OFF appliances. The consumption in winter is generally higher due to the remarkable changes in weather parameters.

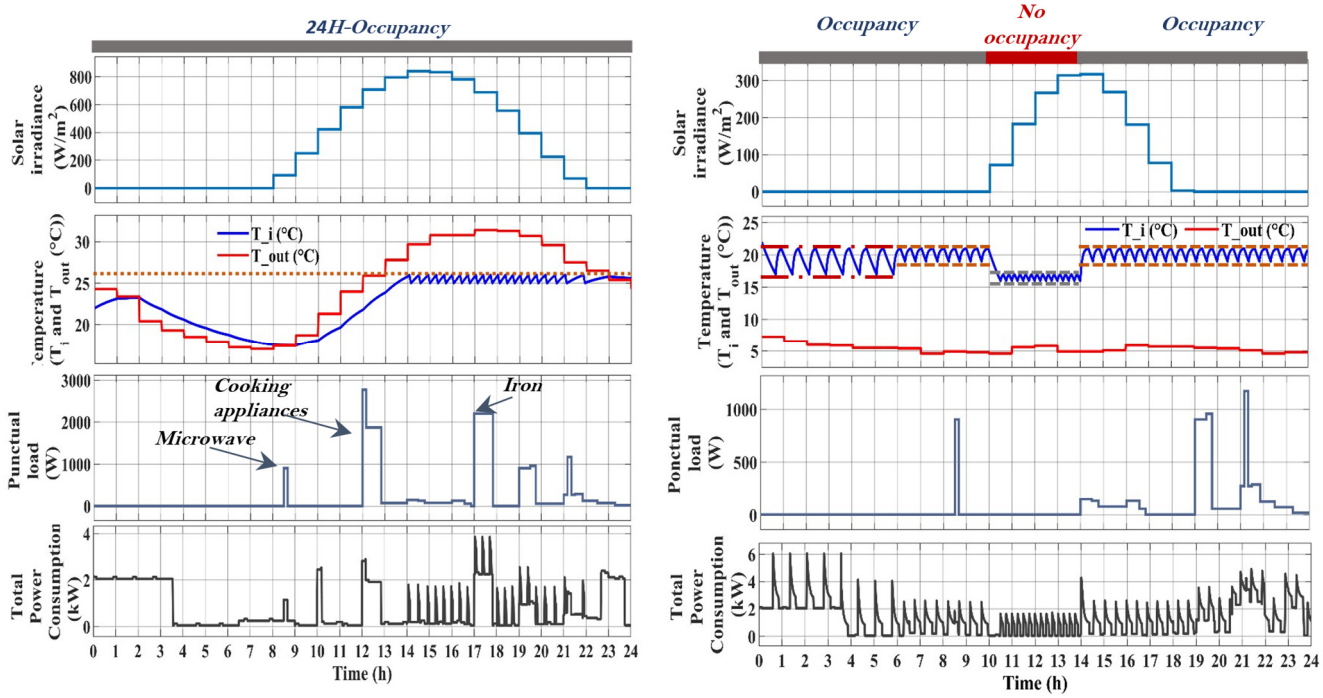

Fig. 1.8. (a) Residential Load Profile with outdoor temperature and solar irradiation in August and (b) Residential Load Profile with outdoor temperature and solar irradiation in January.

Embedded Implementation

To evaluate the practical applicability of the proposed residential load profile generator, a prototype was implemented on a Raspberry Pi 4 integrated with the Home Assistant platform. The objective of this implementation is to demonstrate that the proposed modelling framework can operate on a low-cost embedded system and generate residential load profiles in real time.

As illustrated in Figure 9, the system follows a two-layer architecture. The first layer consists of a web-based interface that allows users to define household characteristics, appliance configurations, and occupancy schedules. Weather forecast data are automatically retrieved through an external API and integrated into the model inputs.

The second layer performs the load profile computation, where the appliance models process the environmental and user-defined parameters to generate a 24-hour electricity consumption profile. The resulting load profile is then displayed through the web interface for visualization and analysis.

The application allows users to:

- Set their location and therefore weather forecast data as well as daytime light used for predicting the load profile are retrieved based on this user-defined input.
- Change and add appliances with accessibility to modify parameters like thermal properties along with nominal power consumption.
- Choose the standard complying with the household insulation. Currently two typical standards are considered, RT 2012 and RT 2020. They are the most commonly adopted in France. However, it is easy to add new insulation standards in the future if needed.

- Modify house configuration (area, ceiling height, number of floors, including the number of windows and doors).
- Specify the number of occupants and their age ranges (adults/children). These inputs have an impact on the hot water consumption for example.
- Specify if the following day is a working day or a holiday (this will affect the considered occupancy profile).
- Select ON/OFF appliances with estimated start time, duration, and frequency of use (if desired).

All these features make the model generic and suitable for different households, with flexibility in parameter adjustments and easy implementation.

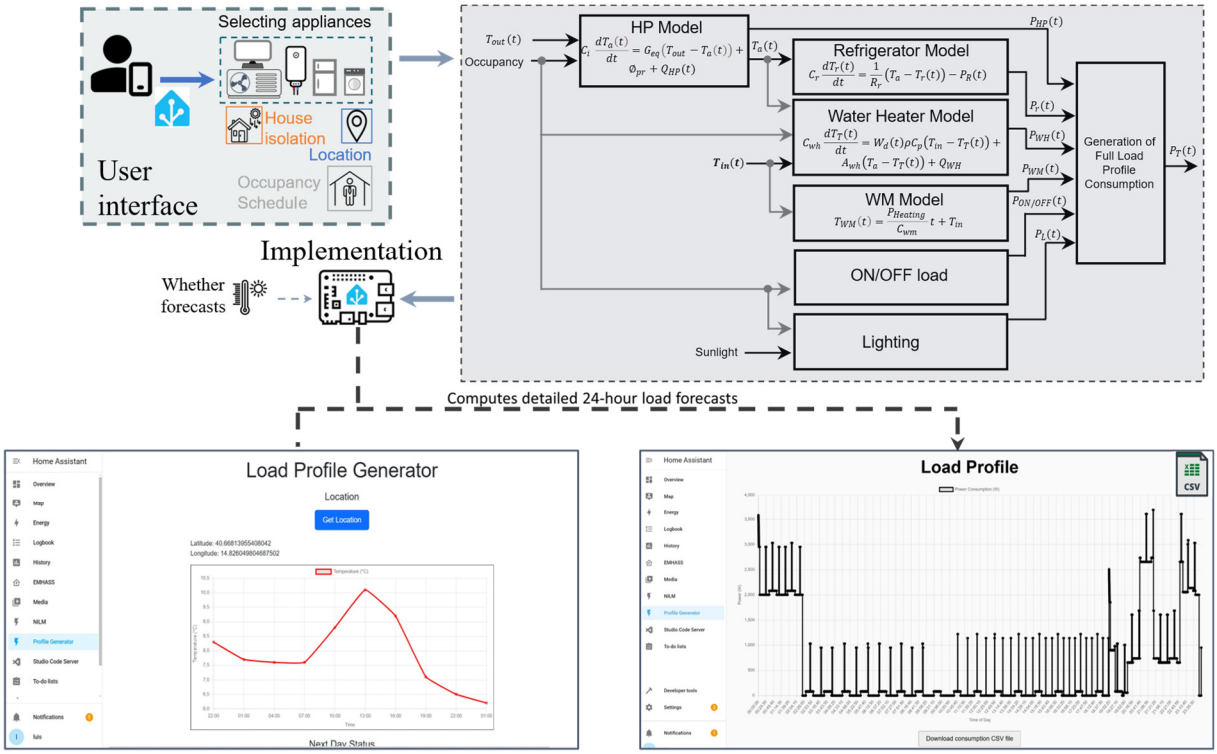

Fig. 1.9. Conceptual workflow for power consumption profile generation.

3.1.4. PV-Battery system modelling & cost assessment

A modelling framework for residential PV–battery systems was developed to represent both system operation and battery degradation. The system model describes the power flows between PV generation, the battery, household loads, and the grid while respecting operational constraints such as power limits, state-of-charge boundaries, and grid exchange limits.

Since the battery is the most degradation-sensitive component of the system, a lifetime model was integrated into the framework. The degradation model considers both calendar aging and cyclic aging, allowing the evolution of the battery State of Health (SoH) to be estimated over time.

In addition, a degradation cost assessment is incorporated to account for the economic impact of battery aging during system operation. This approach enables a more realistic evaluation of system performance by linking short-term operational decisions with long-term battery replacement costs.

Battery degradation model

In recent years, the most commonly used batteries for residential PV-battery systems is lithium-ion batteries, particularly LiFePO4, due to their long lifetime and high efficiency. Hence, this battery is used and evaluated in degradation studies.

The degradation of lithium-ion batteries is typically characterized by two interconnected processes: calendar aging and cyclic aging. Calendar aging refers to the decline in battery performance over time, regardless of usage, while cyclic aging is related to the number of charge-discharge cycles the battery can complete before reaching its end-of-life (EOL).

The overall battery degradation is calculated by combining the effects of calendar aging and cyclic aging at each time step, as shown in Equation (1.12).

$$Q_{t,F} = Q_{t,F}^{cyc} + Q_{t,F}^{cal} \quad (1.12)$$

where $Q_{t,F}^{cyc}$ represents the degradation due to cyclic aging, and $Q_{t,F}^{cal}$ corresponds to calendar aging.

A semi-empirical model for the calendar aging of LiFePO4 batteries is presented in Equation (1.13). This model depends on temperature and SoC. For residential applications, the temperature is typically close to ambient conditions. Therefore, it is fixed at 25°C to analyse the impact of SoC variation alone.

$$Q_{t,F}^{cal}(\mathrm{T}, SoC_t) = (\beta_1 \cdot SoC_t^{\beta_2} + \beta_3)(\beta_4 T^{\beta_5} + \beta_6)d^{\beta_7} \quad (1.13)$$

Where β_1 to β_7 are fitting parameters.

Cycle aging can be modelled as a function of SoC, C-rate, or the energy throughput of the battery. In Equation (1.14), cyclic degradation is expressed based on the energy throughput, taking into account N_b, the number of batteries installed, E_b the energy capacity of each battery and N_{cyc}, the number of battery cycles.

$$Q_{t,F}^{cyc} = 0.5 \frac{\sum P_{t,b} \cdot \Delta t}{N_{cyc} N_b E_b} \quad (1.14)$$

Where $P_{t,b}$ is the battery power at time step t, defined as the charging or discharging power exchanged with the battery. Δt is the time step duration.

Battery lifetime modelling

The battery SoH is modelled based on the capacity fade $Q_{t,F}$. It starts from an initial value $SoH_i = 1$ when the battery is new and unused, and decreases over time as capacity fade increases due to the aging process. The battery reaches its EoL when SoH drops to a final value $SoH_f = 0.8$. As shown in Equation (1.15).

$$SoH_{t,b} = SoH_{t-1,b} - 0.2 \cdot Q_{t,F} \quad (1.15)$$

where 0.2 is the degradation coefficient, such that a complete degradation level (i.e., $Q_{t,F} = 1$) corresponds to a state of health SoH = 0.8, which is considered the EoL threshold SoH_f.

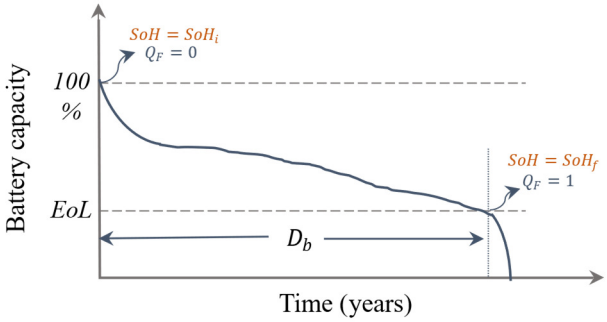

Fig. 1.10. General trend of battery degradation based on time.

To better understand how to model the aging process of batteries, it is important to examine the evolution of their capacity fade over time. Figure 1.10 illustrates the general degradation trend of lithium-ion batteries. The capacity starts at its initial value with zero capacity fade and gradually decreases due to the combined effects of calendar and cyclic aging. Once the battery reaches the EoL threshold, typically defined at 80% of the initial capacity, degradation accelerates rapidly and the remaining capacity becomes unpredictable.

To capture this behaviour, the battery service duration D_b is modeled as a function of annual degradation rate, denoted by A_b, quantifies the yearly reduction in battery capacity due to aging. As given in Equation (1.16).

$$D_b = \frac{SoH_i - SoH_f}{A_b} \tag{1.16}$$

where A_b is the total annual scaled degradation of the batteries is calculated in Equation (1.17).

$$A_b = 0.2 \cdot \beta \sum_{t=1}^{n} (Q_{t,F}^{cyc} + Q_{t,F}^{cal}) \tag{1.17}$$

where β is a scaling parameter that depends on the time resolution of the data used in the optimization either weekly, as in sizing, or daily, as in short-term day-ahead optimization in order to annualize the degradation.

System operation model

From the power flow representation in Figure 1.11, the operation model of the system can be formulated by considering power limitations and physical constraints.

Power constraints must be satisfied at each time step, as the optimization is carried out using real data with a fixed interval Δt over a predefined time horizon.

Limitation on the maximum contracted power exchange between the grid and the system is expressed in equation (1.18) and (1.19).

$$0 \leq P_{t,G\rightarrow(b,L)} \leq P_G^{max} \tag{1.18}$$

$$0 \leq P_{t,(pv,b)\rightarrow G} \leq P_G^{max} \tag{1.19}$$

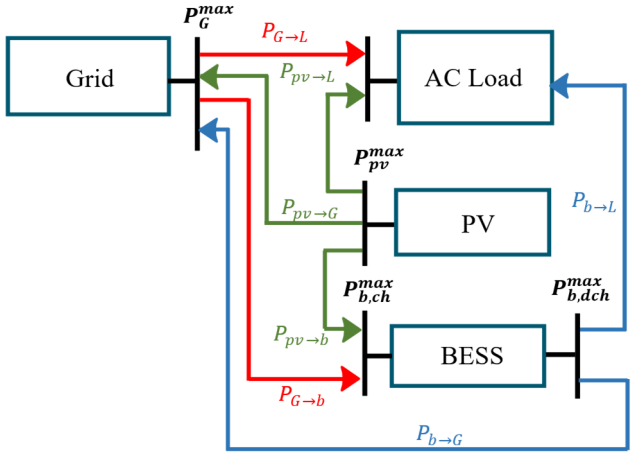

Fig. 1.11. Power flow representation.

Equations (1.20) and (1.21) present models for PV generation, which take into account the solar irradiance incident on the PV modules and their temperature to determine the instantaneous normalized output power.

$$T_{pv}(t) = T_a(t) + \frac{NOCT-20}{800} G(t) \tag{1.20}$$

$$p_{pv}(t) = p_{pv,m}(1 - K_T(T_{pv}(t) - T_s)) \cdot \frac{G(t)}{G_s} \tag{1.21}$$

Where p_{pv} denotes the instantaneous output power of a PV module, while $p_{pv,m}$ refers to its rated power. K_T is the temperature coefficient of the PV cell, T_{pv} is the cell temperature, and T_s is the reference temperature under Standard Test Conditions. G

represents the actual solar irradiance, G_s is the irradiance under STC, T_a is the ambient temperature, and NOCT stands for the Nominal Operating Cell Temperature.

The maximum PV output constraint is defined in Equation (1.22).

$$0 \le P_{t,pv\to(L,b,G)} \le P_{pv}^{max} \tag{1.22}$$

Equation (1.23) presents the battery energy balance, accounting for charging and discharging processes. The term $SoH_{t,b}$ is included to reflect the impact of degradation on the battery storage capacity over time.

$$E_{t,b} = E_{t-1,b} + (\eta_{b,c} P_{t,(pv,G)\to b} - \frac{P_{t,b\to(G,L)}}{\eta_{b,d}})\Delta t \cdot SoH_{t,b} \tag{1.23}$$

The lower and upper bounds of the charging and discharging power of the battery storage unit are defined in Equations (1.24) and (1.25).

$$0 \le P_{t,(pv,G)\to b} \le P_{b,ch}^{max} \tag{1.24}$$

$$0 \le P_{t,b\to(G,L)} \le P_{b,dis}^{max} \tag{1.25}$$

Equation (1.26) defines the SoC of the battery as the ratio of the stored energy $\mathrm{E}_{t,b}$ to the total battery capacity $N_b \mathrm{E}_b$, providing a normalized measure of the battery available energy at a given time. Meanwhile, Equation (1.27) imposes constraints on the minimum and maximum allowable SoC levels.

$$SoC_{t,b} = \frac{\mathrm{E}_{t,b}}{N_b \mathrm{E}_b} \tag{1.26}$$

$$SoC_b^{min} \le SoC_{t,b} \le SoC_b^{max} \tag{1.27}$$

The C-rate of the BESS is determined based on its charging and discharging operations, as shown in Equation (1.28).

$$C_{t,rate} = \frac{\mathrm{P}_{t,b}}{N_b \mathrm{E}_b} \tag{1.28}$$

The constraints on DC-side power limitation, simultaneous battery charging and discharging, and power exchange with the grid are given in Equations (1.29), (1.30), and (1.31), respectively. In addition, the power flow balance to the load is enforced by the constraint in Equation (1.32).

$$P_{t,pv\to(L,G)} + P_{t,b\to(L,G)} \leq P_{DC}^{max} \tag{1.20}$$

$$P_{t,b\to(L,G)} \cdot P_{t,(pv,G)\to b} = 0 \tag{1.30}$$

$$P_{t,G\to(L,b)} \cdot P_{t,(pv,b)\to G} = 0 \tag{1.31}$$

$$P_{t,L} = P_{t,G\to L} + P_{t,b\to L} + P_{t,pv\to L} \tag{1.32}$$

Equation (1.34) represents the energy cost associated with power exchange with the grid. It accounts for the energy consumed from the grid by both the batteries and the loads, calculated according to the ToU tariff. It also includes the energy fed back into the grid, which consists of contributions from both the BESS and the PV system.

$$C_{t,G} = P_{t,G\to(L,b)} \cdot \Delta t \cdot ToU_t - P_{t,(pv,b)\to G} \cdot \Delta t \cdot FiT_t \tag{1.34}$$

where FiT_t is the energy price for selling electricity back to the grid. It represents 80% of ToU_t, excluding applicable taxes.

Day-Ahead Energy Management

For day-ahead operation, the focus shifts to the EMS, which becomes central to optimizing energy flow. The presence of the ER converter enables the dynamic coordination of power exchange between the PV system, BESS, the grid, and the residential load. The proposed EMS is designed to operate over a 24 hours horizon where it predicts both energy consumption and PV generation. These forecasts, combined with day-ahead energy prices, serve as inputs for the day-ahead optimization.

The day-ahead optimization is applied within the household EMS and is structured in two main layers, as shown in Figure 1.12. The upper layer is the EMS, which collects historical system data, integrates weather forecasts, and predicts PV output and electricity demand. Using this information, the optimization problem is solved to determine the most cost-effective strategy for managing energy flow over the next 24 hours. The resulting power references are then sent to the lower layer, consisting of the physical system: the residential load, PV panels, BESS, and the grid, all interconnected via the ER converter, which executes the optimal energy dispatch in real-time operation.

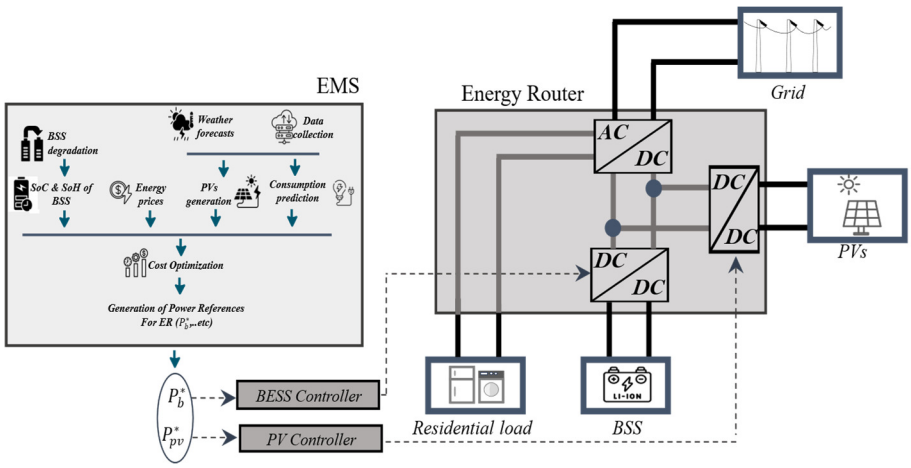

Fig. 1.12. Architecture of the proposed Short-Term EMS.

Day-Ahead optimization

The developed day-ahead optimization strategy aims to minimize the total operation cost of a residential PV-battery system while accounting for short-term battery degradation effects. To ensure the approach realistically captures battery wear in daily operations, the optimization is formulated to be battery aging-aware by integrating degradation cost models directly into the objective function. Several degradation modelling approaches exist in the literature to quantify the impact of battery usage on lifetime, such as SoH-based models that compute cost as a function of SoH loss, and FEC-based models that use Full Equivalent Cycles to estimate degradation. These models are used to link short-term energy management decisions with long-term battery degradation dynamics.

Optimization formulation

The day-ahead optimization problem is formulated to minimize the total operation cost over a 24-hour time horizon with a fixed time step, typically set to 5 minutes. The objective function, presented in (1.35), includes three main components: the cost of electricity purchased from the grid, the revenue from energy exported to the grid, as detailed in Equation (1.34) in the case study and system operation model section, and the degradation cost of the battery $C_{d,F}^{Model}$, which accounts for both calendar and cyclic aging effects, as introduced in the battery degradation model section. This integrated formulation ensures that the optimization not only minimizes daily operational costs but also balances short-term economic benefits with long-term battery health preservation. The optimization is formulated as follows.

$$min\ C_{Daily} = C_{d,F}^{Model} + \sum_{t=1}^{n} C_{t,G} \tag{1.35}$$

$$Subject\ to: \begin{cases} Constraints\ in: (1.18), (1.19), (1.22)\ to\ (1.27), \\ and\ (1.29)\ to\ (1.32) \end{cases} \tag{1.36}$$

The optimization includes all operational constraints previously defined in the system operation model section, covering power balance, maximum power limits, and charging/discharging constraints.

Battery degradation cost modelling

A commonly used approach in EMS is to convert battery degradation into a monetary cost, enabling the integration of long-term battery wear into short-term operational decisions. This formulation helps prevent excessive degradation due to daily cycling and ensures that optimal control strategies account for battery aging.

Two widely adopted models for estimating battery aging costs are the SoH-based model and the (FEC)-based model:

1) SoH-Based Model This approach calculates degradation cost based on the loss in battery SoH over time. The idea is to penalize each loss of SoH proportionally to the initial capital cost of the battery. The total cost over a prediction horizon is given by:

$$C_{d,F}^{SoH} = \sum_{t=1}^{n} \frac{-c_f \cdot N_b E_b}{1 - SoH_f} \Delta SoH_{t,b} \tag{1.37}$$

Where: c_f is the battery cost per kWh [€/kWh], E_b is the nominal capacity of the battery [kWh], $\Delta SoH_{t,b}$ is the SoH degradation during time step t.

2) FEC-Based Model This model assumes that battery degradation is mainly due to the number of charge-discharge cycles. The total battery life is characterized by a predefined number of FECs, after which the battery reaches its end of life. The cost per time step is calculated as:

$$C_{d,F}^{FEC} = \sum_{t=1}^{n} \frac{c_f \cdot N_b E_b}{N_{Cyc}} \Delta FEC_{t,b} \tag{1.38}$$

Where: $\Delta FEC_{t,b}$ is the fraction of a full cycle consumed at time step t.

This approach may underestimate degradation under conditions where calendar aging dominate.

Proposed degradation cost model

Unlike the previous models, the proposed approach incorporates both the physical degradation of the battery and the financial impact of its future replacement by considering the effect of interest rates. This choice is motivated by the fact that in the system sizing stage, the battery replacement cost was discounted using a sinking fund approach, which ensures financial consistency between long-term investment planning and short-term operational decisions.

$$C_{d,F}^{deg-rep} = c_f \cdot N_b E_b \cdot \frac{i_{sa}}{(1+i_{sa})^{\frac{SoH_i - SoH_f}{0.2 \cdot \gamma \cdot Q_{d,F}}} - 1} \cdot \frac{1}{\gamma} \quad (1.39)$$

Where: in the daily case, γ is set to 365, and where:

$$Q_{d,F} = \sum_{t=1}^{n} Q_{t,F} \quad (1.40)$$

This model ensures consistency with the economic assumptions used during the sizing phase and reflects more accurately the financial consequences of battery wear. It is especially useful for applications where the EMS must balance cost savings and asset longevity while respecting financial return criteria.

Seasonal performance analysis of the proposed model

To evaluate the sensitivity of the proposed degradation-integrated cost model to seasonal conditions, the day-ahead optimization was applied to two representative days: one in summer and one in winter (Figure 1.13). These test cases reflect typical consumption behaviours under different environmental and pricing conditions. The optimization problem was solved with a temporal resolution of 5 minutes (Δt = 5 min). Both energy prices and household demand exhibit seasonal variability, winter presents higher consumption and significantly elevated energy tariffs compared to summer. This allows for a comprehensive assessment of how the proposed EMS strategy responds to seasonal fluctuations in both grid dynamics and household energy behaviour, particularly with respect to battery usage, degradation impact, and cost-effectiveness.

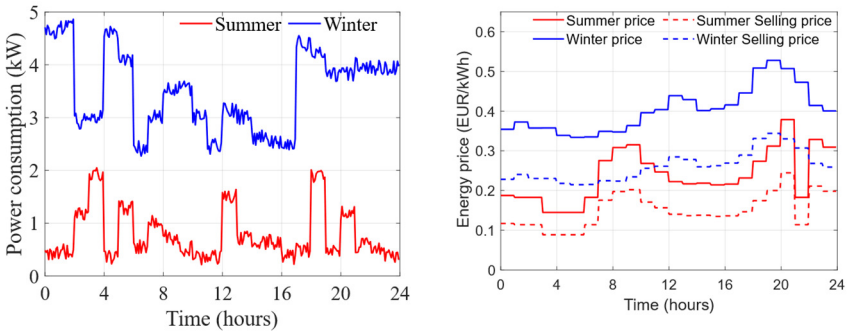

(a) Consumption profiles (b) Energy prices

Fig. 1.11. Seasonal variations in consumption and energy prices.

Figure 1.13-a illustrates the evolution of battery SoH under both winter and summer conditions, starting from the same initial value. As shown, the degradation is more significant in the winter case. This is primarily due to higher energy demand, more intensive cycling, which amplify both calendar and cyclic aging effects. In contrast, the summer scenario demonstrates a slower degradation trend, reflecting less stressful operating conditions for the battery. Figure 1.13-b shows the battery SoC profiles over 24 hours. During winter, the battery reaches its lower SoC limit (SoC_{min} = 0.2), indicating important discharging to meet demand. This increases cycling-related stress. In summer, the battery operates within a narrower and more stable SoC range, benefiting from higher PV generation and lower consumption.

As shown in Table 1.3, the PV-battery system leads to cost savings in both summer and winter scenarios. The Grid-only cost represents the case where all electricity is drawn from the grid without any local generation or storage. The

Final cost excludes the degradation cost, which is treated as a penalty reflecting battery wear. Despite higher degradation in winter, the system yields greater savings due to higher consumption and electricity prices, emphasizing the economic advantage of the proposed day-ahead optimization.

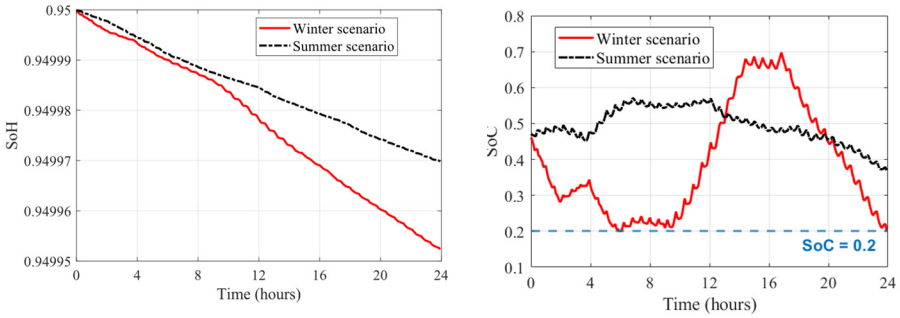

(a) SoH evolution (b) SoC evolution

Fig. 1.14. SoH and SoC profiles for different seasonal scenarios.

Table 1.3: Cost comparison between summer and winter scenarios

Cost component	Summer (€/day)	Winter (€/day)
Imported cost	1.6711	27.2072
Exported cost	- 0.6435	- 0.0030
Battery degradation cost	0.2310	0.4395
Final cost (without degradation)	1.0276	27.2042
Grid-only cost	4.3380	34.0158
Potential savings	1.3104	6.8086

3.1.5. Sizing approach

For sizing PV and BESS in residential applications, the most commonly used approach involves modelling investment, replacement, and maintenance costs over the project lifetime typically 20 years. To integrate operational costs and account for the impact of battery degradation, an annualized cost-based sizing approach is used. In this method, project lifetime costs are converted to equivalent yearly values. This allows annual battery capacity losses to be consistently linked with annual costs, ensuring realistic and comparable optimization results.

The expenses include the cost of PV panels, BESS capacity, and the ER. The PV system lifetime is considered fixed, as it typically exceeds the 20-year (D_{pr}) project duration. The ER is assumed to have a lifespan of 15 years, and its replacement is accounted for accordingly. Therefore, the BESS is the only component whose performance and cost are significantly affected by degradation.

Annualized cost

The total cost includes the initial investment cost, replacement cost, and maintenance cost. Equation (1.41) presents the initial investment cost of the complete system, incorporating the Capital Recovery Factor (CRF) to account for annual loan interest i_L payments on the total cost of all components over M years.

$$C_{Capital} = \sum_j C_{Cap,j} \cdot \frac{i_L(1+i_L)^M}{(1+i_L)^M-1} \cdot \frac{M}{D_{pr}} \quad (1.41)$$

The total initial investment cost $C_{Capital}$ of the system can be broken down by component as follows: Equation (4.42) defines the investment cost of the photovoltaic system, where N_{pv} is the number of PV panels and $C_{Cap,1}$ is the unit cost of one panel.

$$C_{Cap,pv} = N_{pv} \cdot C_{Cap,1} \tag{1.42}$$

Equation (4.43) expresses the battery storage system investment, where N_b is the number of battery units and $C_{b,1}$ is the cost per battery. The ER, acting as the power converter, is assumed to be a single unit with a fixed cost C_{ER}.

$$C_{Cap,b} = N_b \cdot C_{b,1},\ C_{Cap,ER} = C_{ER} \tag{1.43}$$

The replacement cost accounts only for the BESS and the ER and is calculated to cover future replacements. It includes the Sinking Fund Factor (SFF) to determine the periodic deposit required to accumulate the future amount, based on the interest rate of a savings account i_{sa}. The corresponding calculation is shown in Equation (4.44).

$$C_{Replacement} = \sum_j C_{Rep,j} \cdot \frac{i_{sa}}{(1+i_{sa})^{D_j}-1} \cdot \left(1 - \frac{D_j}{D_{pr}}\right) \tag{1.44}$$

The battery replacement cost is calculated based on the number of battery units N_b and the unit cost $C_{b,1}$. Similarly, the ER replacement cost is assumed to be a fixed amount C_{ER}, as shown in Equation (4.45).

$$C_{Rep,b} = N_b \cdot C_{b,1},\ C_{Rep,ER} = C_{ER} \tag{1.45}$$

The annual maintenance cost is estimated as 1% of the capital cost of each component, assuming a uniform maintenance rate across all components, as shown in Equation (4.46).

$$C_{Maintenance} = \sum_j C_{Rep,j} \cdot 1\% \tag{1.46}$$

Joint sizing approach

Once the models for sizing and operating costs are defined, a joint sizing and operation approach can be established. The main idea of this approach is to integrate running costs based on real consumption data, weather conditions, and energy prices for a realistic case study. The optimization problem is then formulated as follows.

$$min\ C_{Tot} = C_{Capital} + C_{Replacement} + C_{Maintenance} + C_{operation} \tag{1.47}$$

$$Subject\ to: \begin{cases} Constraints\ in: (18), (19), \\ (22)\ to\ (27), \\ and\ (29)\ to\ (32) \\ N_{pv} \le N_{pv,max} \\ C_{INV} \le C_{INV,max} \end{cases} \tag{1.48}$$

Where:

$$C_{operation} = \beta \sum_{t=1}^{n} C_{t,G} \tag{1.49}$$

The number of PV panels selected by the optimization must not exceed the available physical space for their installation. Additionally, the initial investment cost is constrained by the maximum budget allocated for the system.

The optimization procedure starts by uploading the input data, including the household consumption profile, corresponding weather data, and the applicable ToU tariff. It proceeds with the initialization of model parameters, such as PV module characteristics and battery specifications.

Throughout the optimization loop, the number of PV panels and the BESS size are selected. For each configuration, power flow is simulated, battery SoC and aging are calculated, and energy costs are evaluated based on real consumption data, weather, and energy prices.

The algorithm computes the total cost, including investment, replacement, maintenance, and operational costs. Constraints such as SoC bounds, power limits, and battery degradation are checked. If all constraints are satisfied and the stopping criteria are met, the optimization converges to the optimal solution. The optimization is handled

using MATLAB fmincon solver with an interior-point algorithm, subject to nonlinear constraints and configured to run in parallel with strict tolerance settings for constraint satisfaction, step size, and optimality. However, the optimization process determines the A_b, creating a trade-off between A_b and the number of batteries N_b. This trade-off is illustrated in Figure 15, which shows the replacement cost as a function of A_b and N_b.

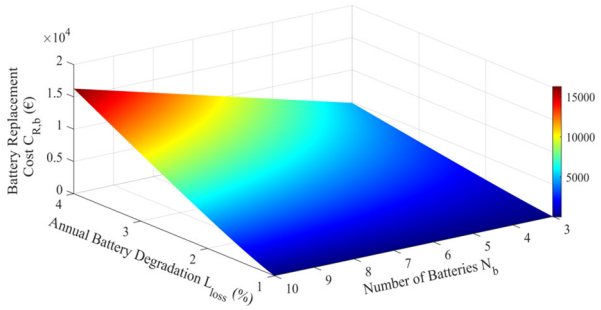

Fig. 1.15. Replacement cost variation with A_b (L_{loss}) and N_b.

The optimization tends to minimize the replacement cost either by selecting a higher number of batteries, which reduces degradation, or by avoiding high A_b values that would result in frequent replacements.

Sizing Results

To evaluate the proposed approach, different scenarios based on solar irradiance levels are considered. Each scenario is built by selecting one representative week of consumption along with the corresponding solar irradiance and temperature data (with a time step of one hour), which is then annualized to serve as input for the optimization process. The objective is to determine the optimal selection of N_b and N_{pv}, along with the associated operational cost, annualized total cost, and corresponding battery lifetime.

Both self-consumption and grid-selling scenarios are analysed to assess the impact of incorporating battery degradation under different conditions and its influence on dynamic lifetime estimation.

Table 1.4 presents the optimization results under three irradiance levels (high, medium, and low) and two operation strategies: self-consumption and selling to the grid.

Table 1.4: Optimization results under different irradiance and selling strategies

	Self Consumption				Selling to the Grid Option			
	N_{pv}^{op}	N_b^{op}	A_b	D_b	N_{pv}^{op}	N_b^{op}	L_{loss}	L_b
High irradiance	24	5	1.58	12.6	25	5	1.59	12.57
Medium irradiance	16	3	1.33	15	25	7	1.37	14.5
Low irradiance	25	7	1.59	12.5	25	7	1.73	11.52

The analysis reveals that irradiance level strongly influences the optimal system configuration. Under high irradiance, a reduced number of PV panels are sufficient for self-consumption (N_{pv}^{op} = 24) compared to low irradiance conditions, which require the maximum number of panels (N_{pv}^{op} = 25). A similar trend is observed for battery sizing. Medium irradiance conditions result in a reduced battery configuration (N_b^{op}= 3), reflecting a favorable balance between energy generation and consumption.

It should be noted that consumption and energy prices also play a significant role in system sizing. In the medium irradiance scenario, the reduced selection of both PV and battery capacity is partly due to lower overall energy demand during the selected period. Additionally, the peak consumption aligns better with the solar generation profile, improving self-consumption efficiency and reducing the need for storage or excess generation capacity.

When grid-selling is enabled, the system tends to size the PV system at its upper bound (N_{pv}^{op} = 25) across all irradiance levels to maximize revenue. This shift comes with an increase in battery usage, especially under medium irradiance (N_b^{op} = 7) compared to only 3 in the self-consumption case. Notably, in the low irradiance case, A_b increases from 1.59% to 1.73% and D_b drops to 11.52 years, indicating that maximizing profit through export comes at the cost of higher battery degradation.

The number of batteries N_b^{op} and the annual degradation rate A_b exhibit a clear inverse relationship. Increasing N_b^{op} helps reduce A_b, thereby extending the battery lifetime D_b, as observed in the medium irradiance case, where N_b^{op} increases from 3 to 7 under the selling scenario. However, in grid-selling scenarios, the system tends to exploit battery cycling more intensively to maximize revenue, resulting in higher A_b and lower D_b, even when N_b^{op} is high.

Table 1.5 presents the cost results for three representative weeks, each associated with a different solar irradiance level and mapped to a corresponding season. Since a typical year is composed of such seasonal variations, this approach provides an estimate of the annual degradation rate A_b and a more realistic evaluation of system performance. For this purpose, all optimization runs were conducted with a fixed number of PV panels N_{pv}^{op} = 25 and batteries N_b^{op} = 7 across all scenarios. These values were selected based on the optimal system sizing identified in the previous table. This setup ensures that the analysis reflects realistic operational conditions throughout the year, focusing specifically on the scenario where selling electricity back to the grid is enabled, which is the adopted case.

Table 1.5: Cost breakdown and battery degradation under fixed PV and BESS configuration

Total capital cost (€/year)	Total maintenance cost (€/year)	Total replacement cost (€/year)	Annual imported energy cost (€/year)	Annual exported energy cost (€/year)	Annual operational cost (€/year)	Overall cost (€/year)	A_b (%)	D_b
516.6	90.75	86.85	4231.23	- 531.28	3700	4394.2	1.47	11.6

The results in Table 1.5 show that, under the fixed configuration, the annual degradation rate A_b is 1.47%, corresponding to a battery lifetime D_b of ap- proximately 13.6 years. These values confirm the effectiveness of the selected system sizing in limiting battery wear while maintaining operational performance throughout the year. The moderate degradation rate ensures fewer replacements, contributing to a balanced trade-off between investment and operational cost.

Figure 1.16 shows the power flow dynamics, battery SoC, and C-rate behaviour over a representative day in the average irradiance scenario with grid selling enabled. The C-rates for both charging and discharging remain below 0.3, indicating moderate battery usage and controlled cycling. The battery is primarily charged during low-tariff periods and discharged during high-tariff periods, reflecting the optimization objective to reduce energy costs and increase revenue through grid export. All operational constraints are respected, including those on power flow and battery SoC, as shown in the figure.

Figure 1.17 illustrates the payback time when considering the option of selling electricity back to the grid. It shows two curves: the first represents the cumulative cost over 20 years when all the energy demand is met only from the grid. The second curve represents the cumulative cost of the PV-BESS system integrated with an energy router. This cost includes the initial investment (distributed over M years), replacement and maintenance costs, as well as operational costs calculated as the cost of energy purchased from the grid minus the revenue from energy sold back to the grid. As shown in the figure, the payback time is approximately 7 years, indicating that the adoption of such a system becomes more economically beneficial in the long term.

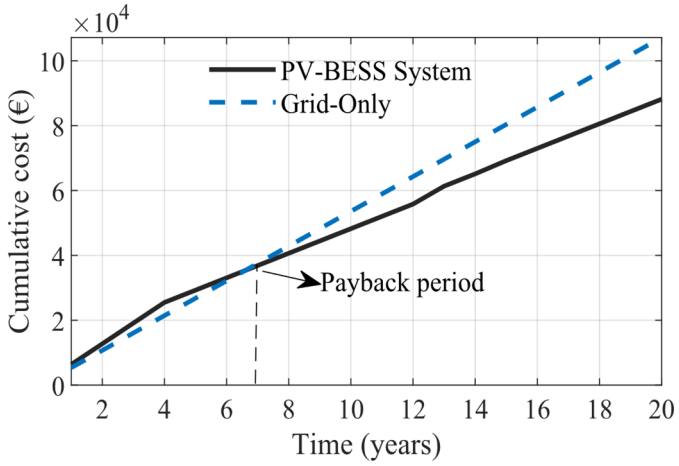

Fig. 1.16. Payback time analysis for PV-BESS System with energy export to the Grid

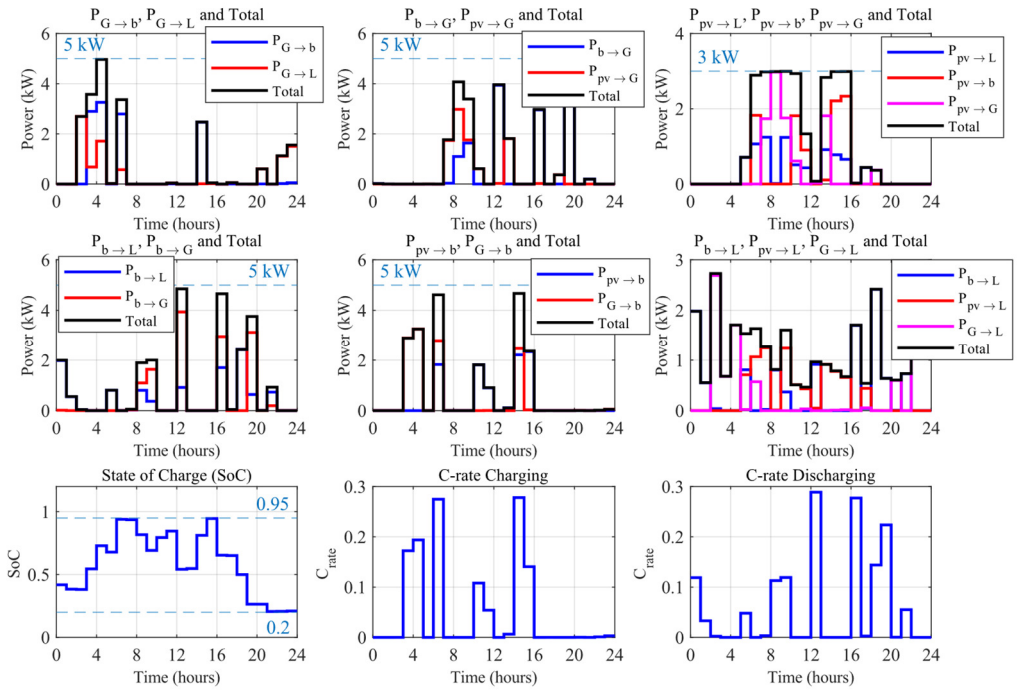

Fig. 1.17. Power flow, SoC, and C-rate profiles for a representative day under average irradiance.

3.1.6. Contribution to the WP objectives

The work contributes to WP4 by providing core modelling and management functions required for prosumer energy systems. First, the residential load profile generator enables prediction of household demand under varying weather and occupancy conditions, which is essential for anticipative energy management. Second, the PV–battery system and battery lifetime models improve the representation of storage behaviour by accounting for operational constraints and degradation effects. Third, the degradation-aware cost assessment and day-ahead optimization framework support more reliable and economically relevant dispatch decisions. Finally, the implementation of the load forecasting tool on Raspberry Pi 4 with Home Assistant demonstrates compatibility with low-cost edge platforms, in line with the objective of developing practical and deployable solutions for prosumer applications.

3.1.7. Scientific achievements

Experimental prototypes

#	Name	Description	Status (designed, assembled, tested)	Photo
	Residential Load Profile Generator	Software application that generates 24-hour residential electricity demand profiles using appliance level models, occupancy schedules, and weather data. The tool is implemented as a web-based interface and deployed on a Raspberry Pi integrated with Home Assistant for EMS applications.	Designed See: https://github.com/Cheikhelkebir/Residential-Load-Profile-Generator	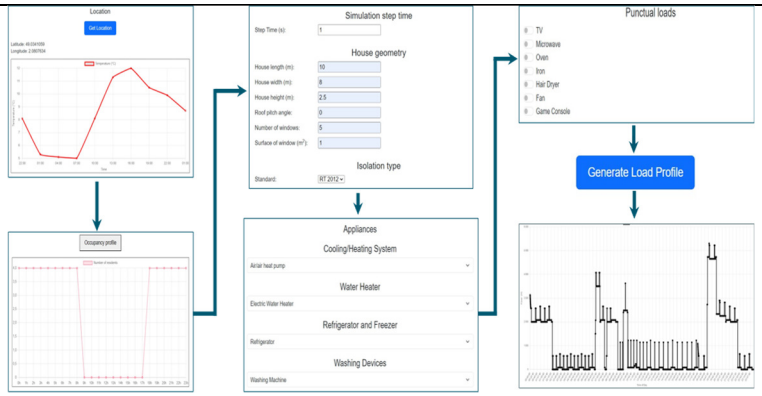 *Figure 1: Load profile simulation process*

Publication

#	Title, incl. citation information	Type (Conference, journal, book chapter)	Status (Submitted, accepted, published)	DOI
1	Generic residential load profile generator based on weather data and occupancy	Journal	published	https://doi.org/10.1016/j.matcom.2025.04.044
2	Joint sizing and energy management optimization with dynamic battery lifetime modeling in residential PV–battery systems	Journal	published	https://doi.org/10.1016/j.renene.2026.125188
3	A Comparative Study of Battery Degradation Cost Modeling in Residential PV-Battery Systems for Day-Ahead Optimization	Conference	published	doi: 10.1109/IECON58223.2025.11221673
4	Programme générateur d'un profil de charge journalier générique dans un contexte résidentiel en combinant les modèles physiques	Conference	published	https://hal.science/hal-05506773/document

	et des données météorologiques			
5	A Unified Hierarchical Digital Twin Platform for Synergistic Management of Low-voltage Electrical Network Components	Conference	published	doi: 10.1109/ISGTEurope64741.2025.11305379
7	Multiparametric Optimization for Residential EMS with an Energy Router and Aging-Aware BESS Considering Variable Ranges for Prediction Accuracy	Conference	accepted	

Others
otypes, simulation diagrams, etc.

3.2. Task 4.2 – IRP10 "Energy Management Systems for Residential Micro-Grids with Integrated Energy Storage"

3.2.1. Introduction

The work on the Energy Management System (EMS) for a residential (droop-controlled DC) microgrid with an Energy Storage System (ESS) was developed, experimentally implemented, and validated at the lab facility of Power Electronics Group, Tallinn University of Technology (TalTech) during the period 01 Nov 2023 – 30 Jun 2025. The main objective of this work was to design an energy management system for a droop-controlled DC microgrid using a minimalistic and efficient approach. During this period, several activities were carried out, including data collection, development of the experimental platform, testing of different control approaches, and publication of related scientific papers. In addition to the laboratory facilities, experiments were also conducted using the specialized DC testbed, the DC Innovation Hub, where the proposed methods were validated using real-life prosumer datasets.

3.2.2. Scientific outcomes

The need for energy management in residential microgrids is significant, as efficient coordination of renewable energy sources and household appliances is essential to achieve the most economical outcomes for prosumers. In recent years, DC microgrids, particularly droop-controlled systems, have attracted considerable attention for the efficiency improvements and operational simplicity they offer compared to conventional AC-based systems. Implementing an Energy Management System (EMS) in such microgrids can further enhance system performance and provide additional benefits to prosumers.

According to existing research, an EMS in a centralized microgrid architecture typically operates within a three-layer hierarchical control structure: the primary layer (converter voltage and current control), the secondary layer (power management and energy storage system management), and the tertiary layer (energy management and optimization).

The development of the EMS for the residential DC microgrid in this work was initiated based on a key concept: modifying the droop control curve using available data sources. To better understand and manage the overall system, a communication, visualization, and data-logging platform was also developed (dashboard in fig.2.1). This platform later served as the foundation for implementing the tertiary-level controller for the microgrid. This platform is currently utilized to monitor different parameters in the DC test lab at TalTech (DC Innovation Hub).

Fig. 2.1. Dashboard of visualization and data-logging platform

The platform operates locally on a low-power Intel N150–based mini-PC. Initially, the system was deployed on a Raspberry Pi 5. Still, it was later replaced due to frequent system lockups caused by brownout issues, as multiple peripherals were connected to the device. The mini-PC runs a headless version of Debian and interfaces with several

peripherals, enabling communication with devices that use different protocols, including RS-485, CAN FD, Zigbee, MQTT, and USART.

Node-RED is used as both the front-end and back-end framework for the platform, enabling real-time monitoring and logging of multiple converters, loads, and environmental sensors (such as temperature and air quality) at approximately 1 Hz. In addition, several Python-based scripts run on the platform to visualize droop curves, converter states, and other system parameters. The platform was later made accessible online through a reverse proxy, enabling remote monitoring and interaction.

Alongside the platform's development, work on the droop-controlled DC microgrid began with a straightforward approach: evaluating the integration of a battery energy storage system to increase self-consumption within the microgrid. Droop control is a way to share current between converters. The concept of droop is that the power output of a converter is proportional to the change in the global parameter (for an AC grid, frequency; for a DC grid, voltage). To implement droop control in DC grid, a virtual resistance (droop coefficient) is added to the converter control. For the case(V-P) the droop coefficient k_p is given below,

$$V_{ref} = k_p P_{conv} + V_{bus} \tag{2.1}$$

A simplified DC microgrid configuration comprising photovoltaic (PV) generation, a battery system, a grid interface converter (active front-end converter), and electrical loads was simulated in MATLAB/Simulink over a full year.

The simulation was based on real household energy consumption data from an Estonian residence, with a 1-minute resolution, which served as the mission profile for both PV generation and load demand. In addition, the battery degradation over time was estimated based on the simulation results. Fig. 2.2 illustrates the yearly energy consumption behaviour used in the analysis.

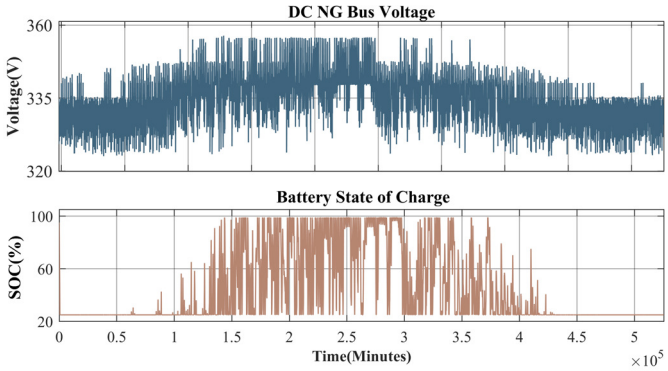

Fig. 2.2. DC bus voltage and Battery SOC over the year

Furthermore, a numerical comparison between AC and DC microgrid configurations was conducted. The results indicated that the DC microgrid with battery storage could reduce life-cycle costs by 15.9%, energy costs by 20.2%, and increase self-consumption by 16.9% compared to the AC-based microgrid system. In addition, state-of-charge (SOC) management for the droop-controlled DC microgrid was implemented using a hysteresis-based control approach. This method was later enhanced by developing an adaptive droop-based strategy, which was modeled and simulated in PLECS. The approach of SOC allocation is shown in fig. 2.3.

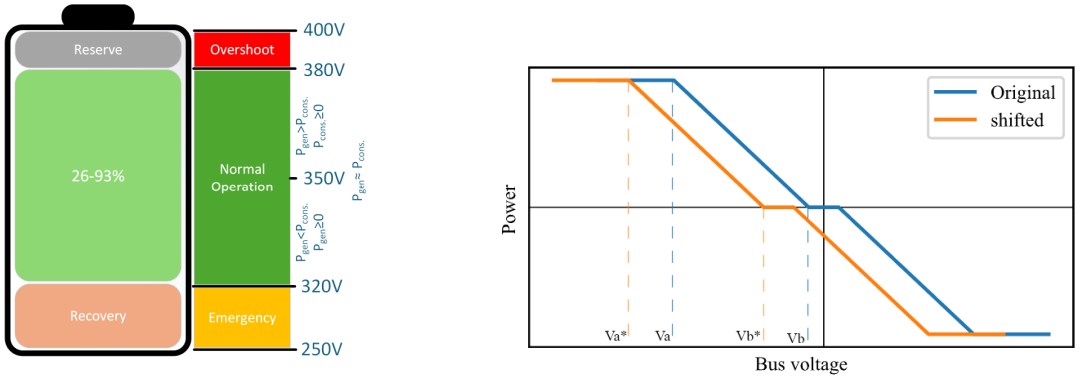

Fig. 2.3. On the left side Battery SOC allocation according to operating voltage range. On the right-side an illustration of symmetrical setpoint shifting to change power sharing among converters

The main objective of this approach was to utilize surplus energy during abnormal DC grid conditions, such as voltage sags and swells, in accordance with Current/OS guidelines. The strategy uses a reserved battery SOC margin to support grid stability: the battery supplies power during voltage sag events and absorbs excess power during voltage swell events, thereby helping maintain a stable DC bus voltage and improving overall microgrid resilience. In fig. 2.4 (left), the normal operation is shown, and in fig. 2.4 (right), the battery operation during sag or swell is shown.

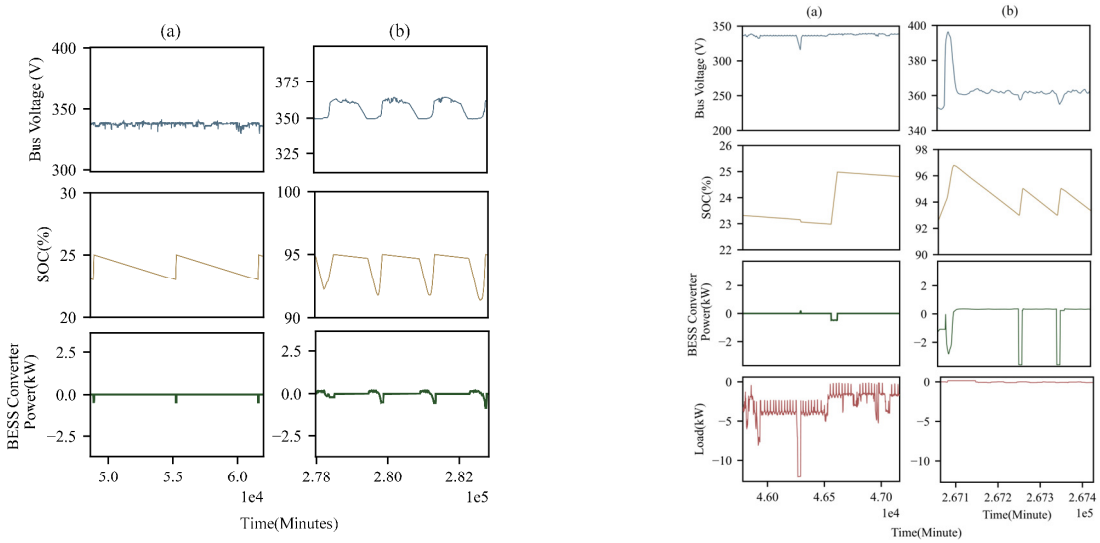

Fig. 2.4. On the left side, the SOC reserve (a) nearing at 25% SOC and SOC recovery at 95% (b) are shown. On the right side of the figure (a), voltage sag and recovery from sag by using reserve battery power, and (b) a voltage swell event happened, and the battery absorbs extra energy to restore voltage to normal

In addition, a centralized Energy Management System (EMS) was developed to achieve power balancing among multiple converters and state-of-charge (SOC) balancing among multiple battery units by adjusting the droop curve setpoints. The proposed method addresses power imbalances between converters that may arise from sensor inaccuracies or measurement errors. To mitigate this issue, one converter is selected as the reference unit, and the remaining converters are calibrated based on information from this reference unit received through the centralized EMS. A symmetrical setpoint shift is used to decrease the power shared by the converter. For the segment of the piecewise droop curve in fig. 2.3 between points V_a and V_b, the droop coefficient is calculated as:

$$k_p = {(V_a - V_b)}/{(P_a - P_b)} \tag{2.2}$$

The corresponding power output would be,

$$P_{out} = P_a + (V_{bus} - V_a) \times \left(\frac{1}{k_p}\right) \tag{2.3}$$

Because the shift is symmetrical, the difference V_a^* and V_b^* is equal to $(V_a^* - V_b^*)$, meaning the k_p value remains unchanged. However, the power output P_{out} changes due to the new values of V_a^* and V_b^*. Secondary control between a 3.5 kW DC-DC partial power converter coupled to a 330 V battery bank and a 350 V DC bus was taken into consideration to evaluate the efficacy of a centralized EMS employing voltage setpoint shifting using MQTT. Fig. 2.5 presents the results demonstrating both power balancing and SOC balancing among identical converters.

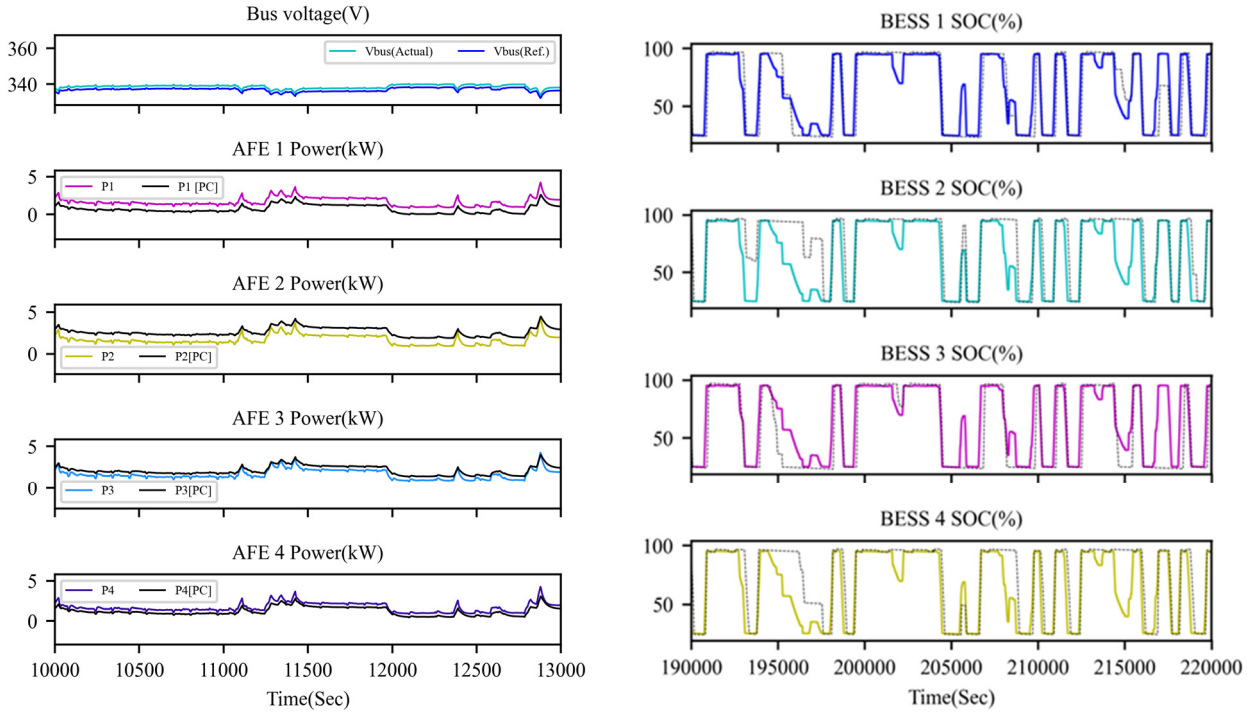

Fig. 2.5. In left side Power balancing by voltage setpoint shifting, where black curves are power variations due to gain error (designated as PC) are shown. Colored lines are balanced power sharing result of voltage sensor error compensation. In right side, SOC balancing by setpoint shifting is shown

In addition, a demonstration of an energy price–based Energy Management System (EMS) was conducted, with droop curve shifting as the control mechanism. The EMS was implemented on the developed platform and utilized to modify the droop parameters of the battery interface converter dynamically. The basic algorithm for the EMS is shown in fig. 2.6 (left) and fig. 2.6 (right) shows the current profiles of the Active Front-End (AFE) converter and the battery interface converter during the period when the droop curve parameters were adjusted by the EMS. This demonstrates how the control strategy influences power flow within the microgrid.

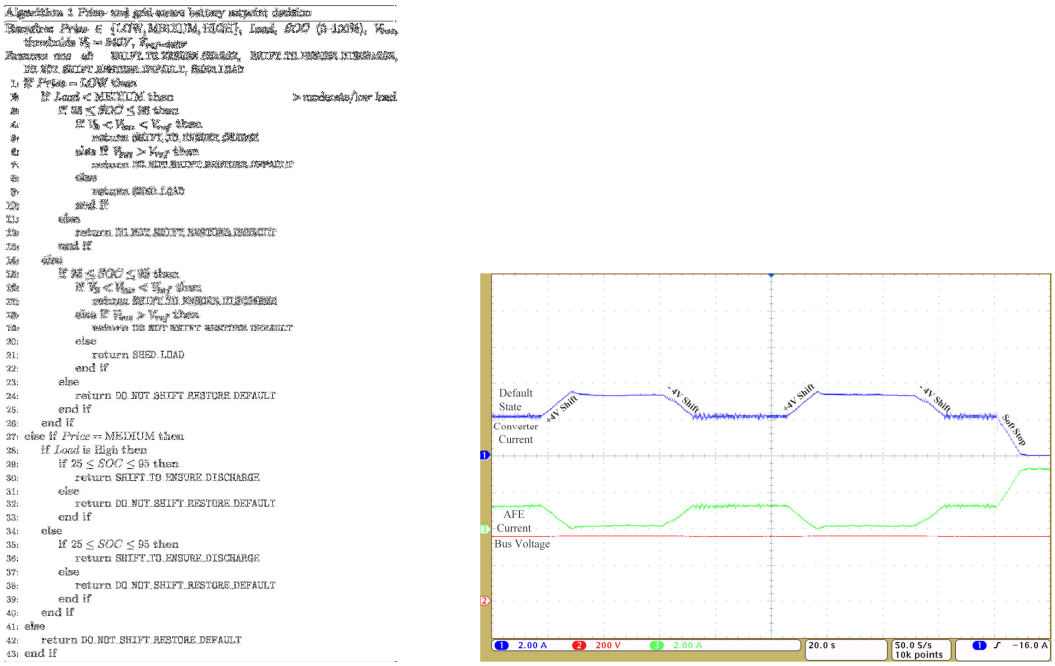

Fig. 2.6. On the left side the basic algorithm is shown and one the right-side oscillogram from experimental setup for testing price-based EMS

3.2.3.Contribution to the WP objectives

The research activities within IRP10 described above collectively address the defined objectives in WP4 related to energy management in residential microgrids. The development of a monitoring, communication, and control platform, along with numerous EMS tactics based on droop curve modification, facilitated the investigation of new approaches to more effectively utilize electric energy. Integrating Energy Storage Systems (ESS) with data-driven control strategies, such as SOC-based management, adaptive droop control, and energy price-based operation, the work demonstrated practical approaches for optimizing energy usage and consumption patterns using both system monitoring and external information sources.

The adoption of a real-time monitoring and logging platform capable of collecting data from converters, loads, and environmental sensors enables enhanced metering and data capture, both critical components of modern smart energy systems. This infrastructure allows for more efficient energy use and serves as the foundation for microgrid decision-making.

Furthermore, the study emphasizes the close collaboration between power electronics and information and communication technologies (ICT) in the creation of Energy Management Systems. The centralized EMS, communication protocols, and data visualization tools demonstrate how ICT can improve coordination across multiple converters, enabling functions such as power and SOC balancing and adaptive control of droop characteristics.

Finally, by incorporating real household energy consumption data and energy price signals, the developed EMS techniques demonstrate how energy applications can adapt to changing external conditions and consumption patterns. Such approaches shed light on energy-related behavioural changes and operational strategies that can enable prosumers to become more involved in energy management and improve their energy consumption.

3.2.4.Scientific achievements

Experimental prototypes

#	Name	Description	Status (designed, assembled, tested)	Photo
1	Online monitoring and logging platform for DC microgrid: dcinnohub.com	A local platform with online access to monitor different parameters with a DC testbed located at TalTech premises, DC residential Innovation Hub. The facility contains various power electronic converters, HVAC equipment, and test equipment. The monitoring platform senses input and output data from converters and environmental sensors via RS-485, MQTT, Zigbee, CAN FD, Ethernet, and USART. The platform is accessible online and based on open-source software.	Tested and running	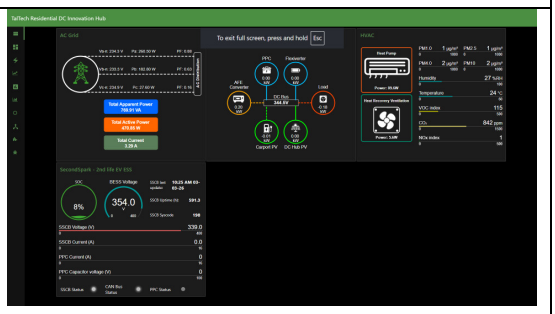
2	Price-Based EMS for DC microgrid	A demonstration microgrid was set up during the ICDCM2025 conference to demonstrate droop curve-shifting-based DC microgrid operation. The droop curve shifting was based on the electricity Price. A partial power converter was used as the BESS converter. The shifting parameters were sent to the converter from EMS using MQTT.	Tested and demonstrated in June 2025	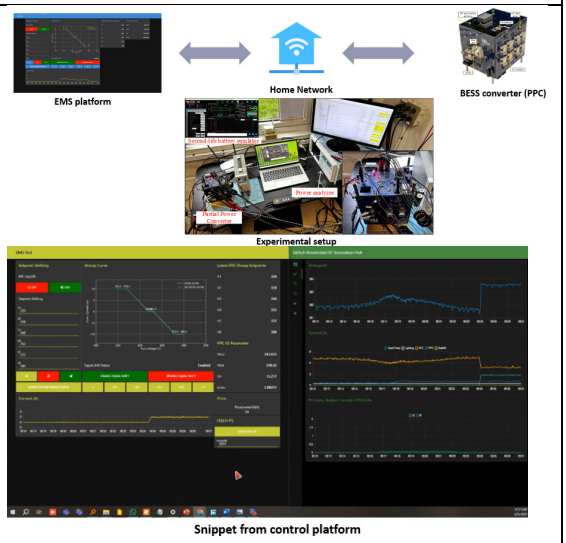

3	Controller Hardware in the Loop (C-HIL)Implementation of DC microgrid	A hardware-in-the-loop model of a DC microgrid was implemented in PLEXIM RT BOX-1. Regarding the controller, the secondary controller was connected to the system via analog I/O. Simulation of BESS management, implementation of observer-based sensor correction, and different EMS cases were performed on the test system. This simulation was later implemented and tested in the DC Innovation Hub.	Tested	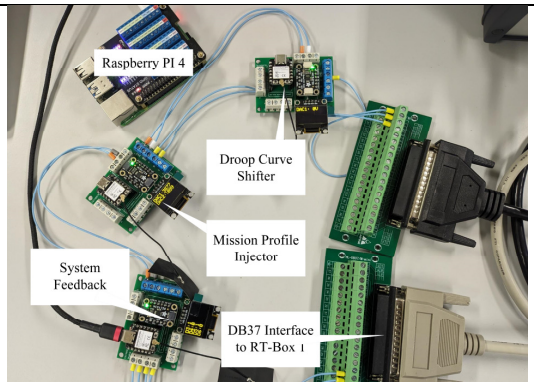 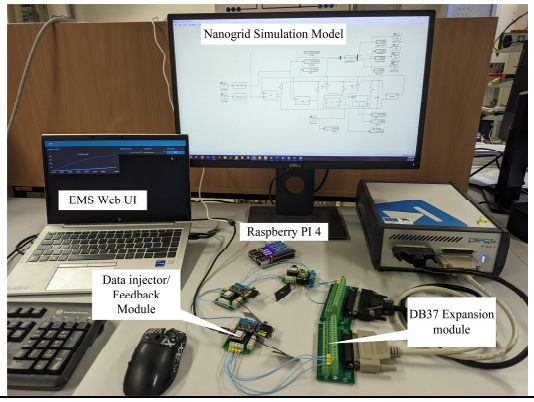

Publication

#	Title, incl. citation information	Type (Conference, journal, book chapter)	Status (Submitted, accepted, published)	DOI
1	S. Hasan, A. Chub, D. Vinnikov, and A. Blinov, "Study of Battery Energy Storage Operation in Droop-Controlled Residential DC Nanogrid," 2024 IEEE 18th International Conference on Compatibility, Power Electronics and Power Engineering (CPE-POWERENG), Gdynia, Poland, 2024, pp. 1-5	Conference	Published	https://doi.org/10.1109/CPE-POWERENG60842.2024.10604364
2	S. Rogowski, S. Hasan, A. Chub, and M. Sibiński, "Assessment of Mixed Energy Storage System Considering High Spatial Resolution Data from a Real PV Installation," *2024 19th Biennial Baltic Electronics Conference (BEC)*, Tallinn, Estonia, 2024, pp. 1-6	Conference	Published	https://doi.org/10.1109/BEC61458.2024.10737964
3	S. Hasan, A. Chub, A. Blinov, and D. Vinnikov, "Implementation Issues of Droop Controlled DC Nanogrids: State of	Conference	Published	https://doi.org/10.1109/RTUCON62997.2024.10830832

	Charge Management of Battery Energy Storage and Impact of Sensor Gain Tolerance," 2024 IEEE 65th International Scientific Conference on Power and Electrical Engineering of Riga Technical University (RTUCON), Riga, Latvia, 2024, pp. 1-6			
4	N. Yadav, S. Hasan, I. Galkin, and A. Chub, "Performance Analysis of Partial Power Converter in DC Microgrid with Active Front-End Converter," 2025 IEEE Seventh International Conference on DC Microgrids (ICDCM), Tallinn, Estonia, 2025, pp. 1-5	Conference	Published	https://doi.org/10.1109/ICDCM63994.2025.11144718
5	S. Hasan, A. Chub, N. Yadav, A. Blinov, J. Kurnitski, and D. Vinnikov, "Energy Management Implementation Approach for Droop-Controlled Residential DC Nanogrids," 2025 IEEE Seventh International Conference on DC Microgrids (ICDCM), Tallinn, Estonia, 2025, pp. 1-5	Conference	Published	https://doi.org/10.1109/ICDCM63994.2025.11144665
6	N. Hassanpour, A. Chub, A. Blinov, N. Yadav, S. Hasan, and D. Vinnikov, "Protection of Bidirectional Step-Up/Down Partial Power Converter against Short Circuit and Open Circuit Faults and Mode Transition Issues," *2024 IEEE 18th International Conference on Compatibility, Power Electronics and Power Engineering (CPE-POWERENG)*, Gdynia, Poland, 2024	Conference	Published	https://doi.org/10.1109/CPE-POWERENG60842.2024.10604315
7	Rogowski, S., Hasan, S., Chub, A. and Sibiński, M. 2025. Enhancement of residential PV energy storage system by supercapacitor battery –	Journal	Published	https://doi.org/10.3176/proc.2025.2S.01

	high spatial resolution data analysis. Proceedings of the Estonian Academy of Sciences,74(2S), 269–280			
8	Hasan, S., Blinov, A., Chub, A. et al. Solar PV Generation and Consumption Dataset of an Estonian Residential Dwelling. Sci Data 12, 481 (2025)	Journal	Published	https://doi.org/10.1038/s41597-025-04747-w
9	S. Hasan, N. Yadav, A. Chub, A. Blinov, and D. Vinnikov, "A Centralized Energy Management System for Droop Controlled DC Nanogrids Using Binary Setpoint Shifting," in Compilation of selected SMARTGYsum project scientific results, in Smart and Green Energy Systems. , pp. 165–179.	Book Chapter	Published	ISBN: 978-84-09-81019-2

3.3. Task 4.3 – IRP11 "On-line diagnosis and optimization of Energy Management Systems for Smart Buildings"

3.3.1. Introduction

IRP11 addresses a central limitation of practical energy management systems for smart buildings: most control and optimization strategies require internal information about demand and generation that is not directly observable from standard field measurements. In realistic residential and tertiary environments, the available measurements are often limited to aggregate electrical power at the point of common coupling and, in the presence of photovoltaic generation, a reduced set of inverter-side or current-voltage data. Under these conditions, advanced energy management requires an intermediate intelligence layer capable of transforming raw measurements into physically meaningful indicators.

The scientific work developed in IRP11 establishes this intelligence layer along two complementary directions. The first direction concerns demand-side intelligence, where aggregate active power is disaggregated into appliance-level information through a robust and computationally efficient non-intrusive load monitoring framework. The second direction concerns supply-side intelligence, where current-voltage measurements of photovoltaic generators are converted into diagnostic parameters able to reflect mismatch conditions and degradation-sensitive trends. The two contributions are then integrated into a unified edge-computing platform, demonstrating that demand-side and supply-side monitoring can operate concurrently in a realistic embedded environment.

The research addresses three practical constraints that frequently prevent the transfer of advanced methods into real energy management systems. First, the algorithms must operate with low-frequency or imperfect measurements rather than ideal laboratory-grade sensing. Second, they must remain robust in the presence of unknown loads, non-uniform photovoltaic operating conditions, and other sources of model mismatch that are unavoidable in the field. Third, they must be deployable on low-cost embedded hardware without requiring external cloud computation or specialized instrumentation for routine operation.

From the perspective of WP4, the relevance of IRP11 lies in the production of actionable monitoring for smart-building energy systems. Demand-side intelligence provides appliance-level power estimates, base-load indicators, and unknown-load information that are directly useful for behavioral feedback, flexibility assessment, and future scheduling strategies. Supply-side intelligence provides physically interpretable model parameters that can support photovoltaic supervision, mismatch analysis, and degradation-oriented diagnosis. The combined platform therefore contributes a foundation for the next layer of energy management functionalities, where diagnosis, optimization, and user interaction need to coexist in a single digital environment. These scientific outcomes have been obtained during 36 months in the facilities of the DIEM research group of the University of Salerno and the SATIE group of Cergy Paris University.

The scientific outcomes are presented in three coherent parts: demand-side intelligence, supply-side intelligence, and practical implementation of the integrated proposal. The subsequent sections explain how these outcomes contribute to the objectives of WP4

3.3.2. Scientific outcomes

3.3.3. Demand-side intelligence for smart-building energy management

The demand-side contribution of IRP11 is structured in two consecutive steps. The first step analyses the transfer capabilities of deep-learning NILM models based on Seq2Seq and Seq2Point convolutional neural networks when the test aggregate includes appliances that were not present during training. The second step introduces the O2RE framework as a practical alternative specifically designed to overcome the limitations revealed by that analysis under realistic edge-deployment conditions.

A first relevant result is therefore the evaluation of Seq2Seq and Seq2Point CNN architectures under increasing domain shift. In these methods, one network is trained per appliance and receives a fixed-length window of aggregate power as input. Seq2Seq predicts the whole target window, while Seq2Point predicts only the midpoint of the window. Both approaches can provide strong accuracy under benchmark conditions, but their transferability is limited when the aggregate signal in the test environment contains unseen appliances or consumption patterns that were not represented in the training domain. The analyzed architectures are illustrated below.

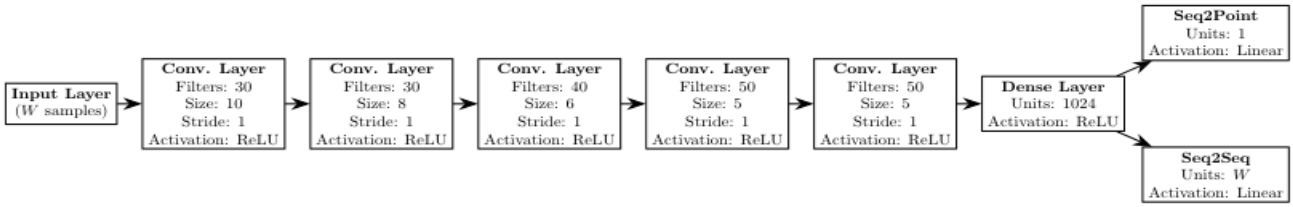

Fig. 3.1. Architectures for sequence-to-point and sequence-to-sequence neural networks

The theoretical analysis of these CNN-based methods shows that the additional disaggregation error caused by unseen loads depends on two coupled factors: the magnitude of the unknown contribution added to the aggregate input and the local sensitivity of the neural model around the evaluated operating point. In practical terms, appliances with low-power states or complex patterns require higher model sensitivity and therefore become more vulnerable to domain shift. This result is important because it explains why strong benchmark performance does not necessarily imply robust field behaviour in real residential environments [7].

The experimental evaluation confirms this limitation. Seq2Seq and Seq2Point were tested on REDD-1, UKDALE-2, and UKDALE-5 by creating increasingly noisy aggregate signals through the progressive addition of non-monitored appliances. The resulting overall estimation accuracy and overall F-measure are reported below for the three datasets.

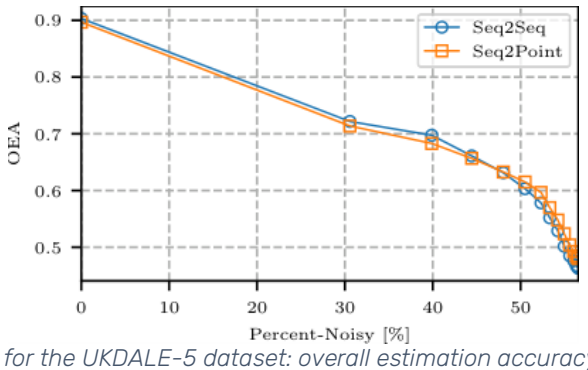

Fig. 3.2. Robustness to noise for the UKDALE-5 dataset: overall estimation accuracy as percent-noisy increases

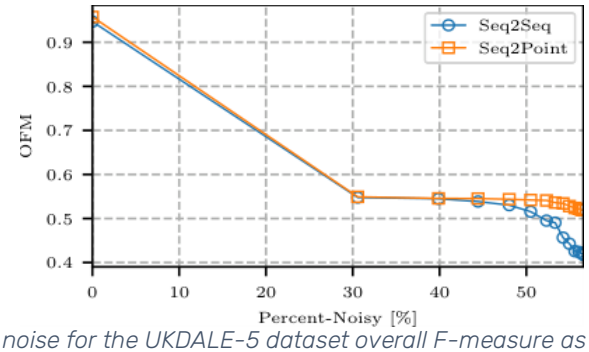

Fig. 3.3. Robustness to noise for the UKDALE-5 dataset overall F-measure as percent-noisy increases

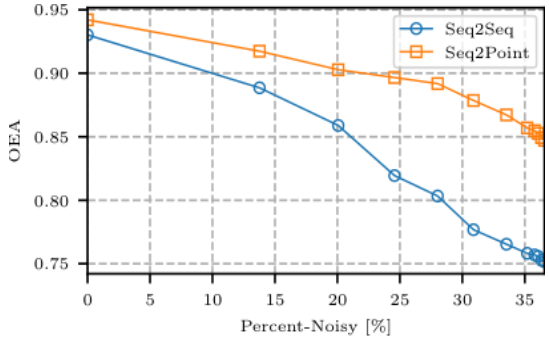

Fig. 3.4. Robustness to noise for the UKDALE-2 dataset: overall estimation accuracy as percent-noisy increases

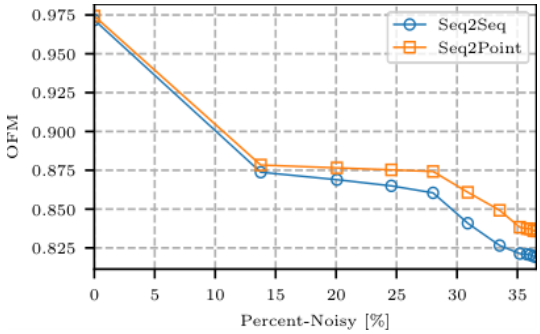

Fig. 3.5. Robustness to noise for the UKDALE-2 dataset: overall estimation accuracy as percent-noisy increases

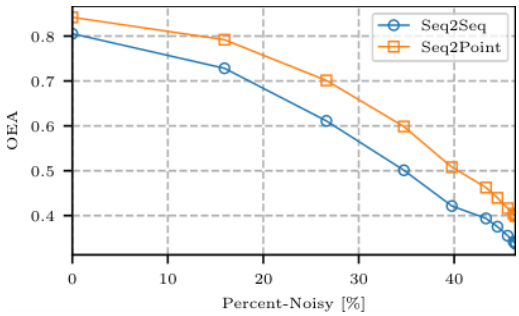

Fig. 3.6. Robustness to noise for the UKDALE-2 dataset: overall estimation accuracy as percent-noisy increases

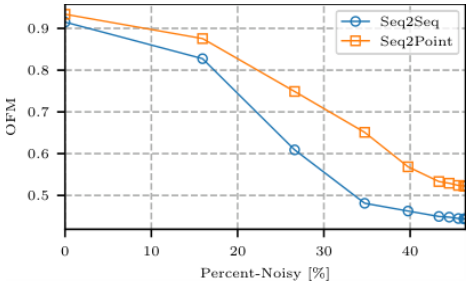

Fig. 3.7. Robustness to noise for the UKDALE-2 dataset: overall estimation accuracy as percent-noisy increases

Across the evaluated datasets, the performance of both CNN architectures decreases as the percent-noisy increases. The degradation is especially severe for appliances with low-power states or complex operating patterns, whereas high-power and more stereotyped appliances are less affected. This behaviour confirms that direct regression from aggregate windows to appliance power is highly dependent on the aggregate patterns seen during training. As a consequence, the deep-learning analysis establishes a clear practical requirement for smart-building NILM: the method must remain robust to unknown loads and domain shifts without assuming the availability of submetered data or retraining in the deployment site [7].

The first scientific outcome of IRP11 is therefore completed by an online non-intrusive load monitoring framework conceived to recover useful demand-side monitoring from the aggregated active-power signal available in a smart building under those realistic constraints. The objective is not only to estimate the consumption of individual appliances, but also to distinguish the contribution of permanently connected background loads and to preserve robustness when part of the aggregate demand is produced by devices that are not explicitly modelled. This formulation is more consistent with real smart-building conditions than conventional NILM approaches based on a closed and perfectly known appliance set [8].
The aggregate active power is represented in our work as

$$P(t) = \sum_{i=1}^{N} p_i\,(t) + B(t) + \eta(t) \qquad (3.1)$$

where (pi(t)) is the power consumed by the (i)-th monitored appliance, (B(t)) represents the base-load contribution associated with always-on or slowly varying devices, and (η(t)) accounts for measurement noise and non-monitored fluctuating loads. The explicit introduction of (B(t)) is essential because the aggregate signal measured in residential buildings systematically contains a non-negligible background component that cannot be assigned to the set of target appliances.

Each appliance is modelled as a finite-state machine, so that the state of appliance (i) is described by the binary variable

$$S_{i,j} = \begin{cases} 1 & \text{if appliance } i \text{ operates in state } j \\ 0 & \text{otherwise} \end{cases} \quad (3.2)$$

with the exclusivity constraint

$$\sum_{j=0}^{M_i} S_{i,j} = 1 \qquad \text{for each appliance } i \quad (3.3)$$

The aggregate power can then be written as

$$P(t) = \sum_{i=1}^{N} \sum_{j=0}^{M_i} S_{i,j}\,(t) P_{i,j} + B(t) + e(t) \quad (3.4)$$

and the instantaneous error is expressed through

$$|e(t)| = \left| P(t) - B(t) - \sum_{i=1}^{N} \sum_{j=0}^{M_i} S_{i,j}\, P_{i,j} \right| \quad (3.5)$$

If Equation (3.5) were minimized directly at each sample, unknown loads would tend to be absorbed by unrealistic combinations of monitored appliance states. Moreover, low-frequency measurements would make the solution highly sensitive to simultaneous or spurious transitions. For this reason, the proposed method does not rely on a purely combinatorial matching stage. Instead, it combines edge detection, probabilistic transition assessment, and state refinement, leading to the Online Real-Time Robust and Edge-Driven (O2RE) framework.

The finite-state appliance representation adopted by the method is shown below.

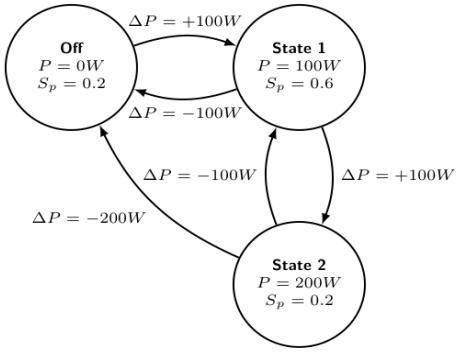

Fig. 3.8. Finite-state representation used for appliance modelling in the demand-side intelligence framework

The operation of the framework is organized around the identification of significant steady-state changes in the aggregate signal and the recursive update of a state-probability structure. Instead of forcing an immediate deterministic interpretation of every power variation, the method preserves multiple admissible hypotheses and progressively rejects inconsistent ones. This mechanism is one of the key reasons why the framework remains robust under unknown-load activity and noisy aggregate conditions. The general O2RE framework is summarized below.

```
//Initialization
S_P ← InitializeStateProb()
S ← None
B ← ∞
for each t do
    //Edge and Base load detection (Module 1)
    P̄_curr P̄_prev ← UpdateSteadyStates()
    E ← P̄_curr − P̄_prev
    B ← UpdateBaseLoad()
    //State Probabilities Update (Module 2)
    state_prob_updated ← False
    if |E| > θ then
        S_P ← UpdateStateProb()
        state_prob_updated ← True
    end if
    E[P] ← Σ_{i=1}^{N} Σ_{j=0}^{M_i} S_{P_{i,j}} · P_{i,j}
    P_fluc ← max(P̄_curr − B, 0)
    //State Probabilities Tune (Module 3)
    if E[P] > P_fluc then
        S_P ← TuneStateProb()
        state_prob_updated ← True
    end if
    //States Prediction (Module 4)
    if state_prob_updated == True or S is None then
        S ← PredictStates()
    end if
    output S as the prediction for time t
end for
```

← : Assignation, //: Section comments,

Fig. 3.9. Finite-state representation used for appliance modelling in the demand-side intelligence framework

The characteristic quantity used to detect an event is the edge between two steady states,

$$E = \overline{P}_{\text{curr}} - \overline{P}_{\text{prev}} \tag{3.6}$$

while the identification of stable operating regions relies on the local mean and variance of the incoming aggregate signal,

$$\mu_P(t) = \frac{1}{3}\sum_{i=1}^{3} P\,(t - i\Delta t) \tag{3.7}$$

$$\sigma_P^2(t) = \frac{1}{3}\sum_{i=1}^{3}(P(t - i\Delta t) - \mu_P(t))^2 \tag{3.8}$$

This event-driven stage isolates the meaningful transitions while filtering short fluctuations that should not trigger a state update. Once an edge has been detected, the method compares it with the expected transitions of the modelled appliances. To improve robustness, the transition amplitudes are processed through the transformed quantity

$$\Delta\tilde{P}_{i,j,k} = \text{sgn}(\Delta P_{i,j,k})\ln\left(|\Delta P_{i,j,k}|\right) \tag{3.9}$$

and the associated likelihood is evaluated using

$$L(E \mid T_{ijk}) = \frac{1}{\sqrt{2\pi}}\exp\left(-\frac{x_{ijk}^2}{2}\right) \tag{3.10}$$

An additional likelihood term is introduced for transitions that cannot be reliably explained by the monitored appliance set,

$$L(E \mid \text{UnkTrans}) = \delta \tag{3.11}$$

where (δ) defines the density assigned to unknown events. This explicit unknown-transition mechanism is a central scientific contribution of the proposed NILM framework. It prevents the method from over-interpreting the aggregated signal and allows the disaggregation process to remain credible when the measured power includes appliances outside the monitored set.

The state-probability structure obtained after each event is further combined with a refinement stage that exploits the expected aggregate power

$$\mathbb{E}[P] = \sum_{i=1}^{N} \sum_{j=0}^{M_i} S_{P_{i,j}} P_{i,j} \quad (3.12)$$

to guide the search toward physically plausible appliance combinations. In this way, temporal coherence is preserved without resorting to computationally intensive exhaustive searches.

The method was validated using representative NILM scenarios built from the REDD and UK-DALE datasets. The monitored appliance states considered in the experiments are summarized below.

Table 3.2: Appliance states used in the NILM experiments

Dataset	Appliance (**Acr.**)	On-States [W]
REDD-1	fridge (**F**)	190, 230
	dish washer (**DW**)	225, 1115
	microwave (**MW**)	1520
	electric oven (**EO**)	3350, 4090
	washer dryer (**WD**)	450, 2700
UKDALE-2	fridge (**F**)	90
	dish washer (**DW**)	100, 2000
	microwave (**MW**)	1308
	kettle (**K**)	2940
	rice cooker (**RC**)	400
UKDALE-5	fridge (**F**)	108
	dish washer (**DW**)	94, 1665
	microwave (**MW**)	1505
	electric oven (**EO**)	2120
	kettle (**K**)	2900

The test scenarios used to assess the proposed framework under realistic conditions are given below.

Table 3.2: NILM test-scenario description

Scenario	Dataset	Test start	Test hours	Percent-Noisy
1	REDD-1	2011-05-14	96	44
2	UKDALE-2	2013-06-01	720	59
3	UKDALE-5	2014-08-20	72	72

The first set of results concerns the appliance-level performance obtained in Scenario 1. The reported estimation accuracy and F-measure confirm that the framework achieves a reliable disaggregation of the target appliances under realistic aggregate conditions.

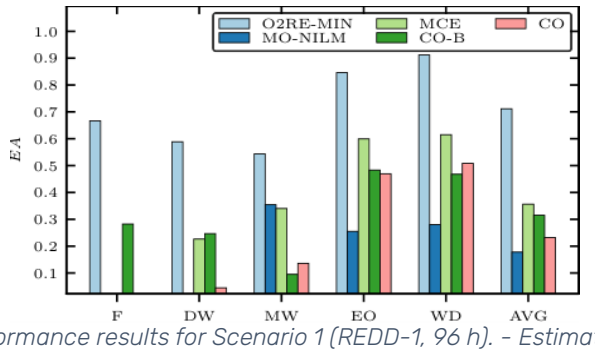

Fig. 3.10. Performance results for Scenario 1 (REDD-1, 96 h). - Estimation accuracy

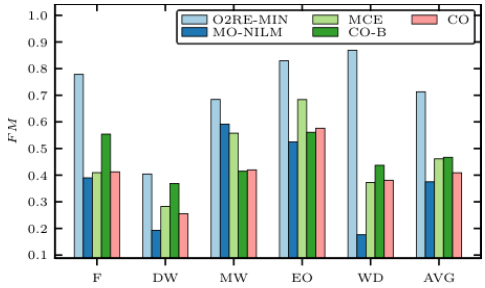

Fig. 3.11. Performance results for Scenario 1 (REDD-1, 96 h). - F-measure

An equally important outcome is the robustness obtained when the aggregate demand contains increasing contributions from non-monitored appliances. This condition is decisive for smart-building operation, because field measurements rarely correspond to a perfectly closed appliance inventory.

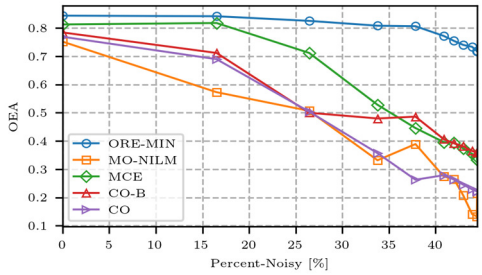

Fig. 3.12. Robustness of the demand-side intelligence framework as the percent-noisy contribution increases. - Overall estimation accuracy

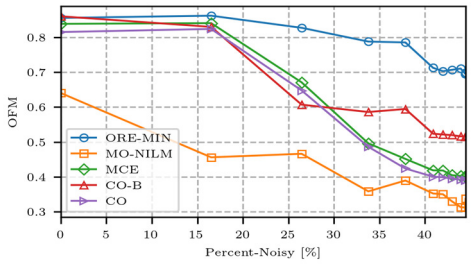

Fig. 3.13. Robustness of the demand-side intelligence framework as the percent-noisy contribution increases. - Overall F-measure

The results show that the proposed framework maintains a coherent performance trend even when the noisy portion of the aggregate signal becomes dominant. This behaviour follows directly from the scientific choices introduced in Equations (3.9) to (3.11): the transition-likelihood transformation, the probabilistic state update, and the explicit handling of unknown transitions. Consequently, the demand-side contribution of IRP11 is not limited to disaggregation accuracy under benchmark conditions; it provides a robust electrical observability layer that remains meaningful in realistic smart-building environments [8].

3.3.4. Supply-side intelligence for photovoltaic diagnosis

The second scientific outcome of IRP11 is a diagnosis-oriented photovoltaic parameter-identification method for operating conditions affected by mismatch. In standard single-diode approaches, the photovoltaic module is treated as if all its cells were exposed to the same irradiance and temperature. This assumption is often not satisfied in practice. Partial shading, soiling, surrounding obstacles, non-uniform reflections, and cell-to-cell dispersion distort the current-voltage characteristic and may force conventional uniform models to compensate the mismatch through physically inconsistent parameter values [9].

Representative mismatch situations are illustrated below.

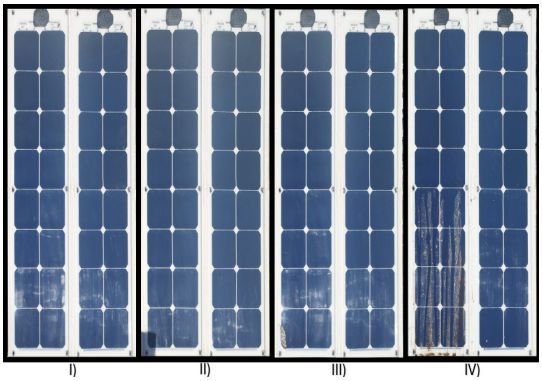

Figure 14. Representative mismatch situations affecting photovoltaic modules in field operation, including non-uniform radiation, surrounding-object shading, bird droppings, and soiling.

A first relevant point is that the uniformity assumption may fail even when the mismatch is not visually obvious in the measured current-voltage curve. In these conditions, fitting a conventional SDM to the full curve or to a restricted region near the maximum power point leads to significantly different parameter estimates, which is an indication that the model structure does not have enough degrees of freedom to represent the underlying physics [10].

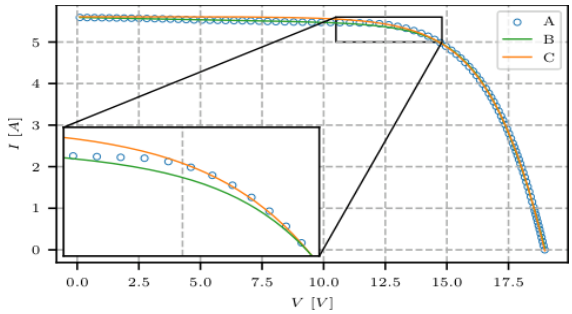

Figure 15. Uniform-assumption limitations. A. Experimental data; B. SDM fitting using the full experimental points; C. SDM fitting using only the points with voltages between $V_{mpp} - 0.2V_{mpp}$ to V_{oc}.

The parameter inconsistency observed in this example is summarized below.

Table 3.3. Uniform-assumption limitations. B. SDM fitting using the full experimental points, C. SDM fitting using only the points with voltages between $V_{mpp} - 0.2V_{mpp}$ to V_{oc}.

Fitting	$I_{ph}[A]$	$I_s[A]$	η	$R_s[\Omega]$	$R_{sh}[\Omega]$
B	5.6029	4.8474e-06	1.4934	0.17562	93.121
C	5.6089	9.5054e-05	1.8901	0.090265	∞

This behaviour motivates the proposed adaptive Double Single-Diode Model. Instead of forcing the whole module to operate under a single effective irradiance, the cells are separated into two groups associated with lower and higher irradiance conditions. This representation preserves a compact equivalent-circuit structure while allowing the model to account for small mismatches that are very relevant for diagnosis but difficult to detect directly from the global curve [10].

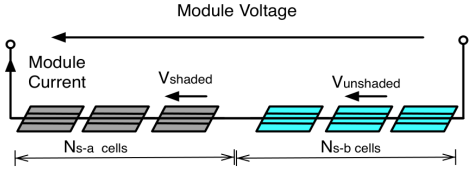

Figure 16. Two-irradiance-level assumption adopted for the photovoltaic module, separating the cells into groups operating under lower and higher effective irradiance.

The equivalent circuit of the proposed D-SDM is reported below.

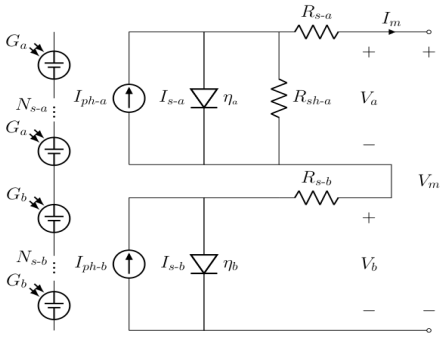

Figure 17. Double Single-Diode Model used for photovoltaic diagnosis, representing two effective cell groups connected in series.

For reference, the single-diode circuit that constitutes the modelling basis of each effective group is also included.

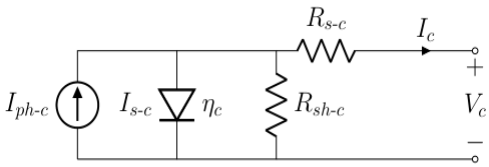

Figure 18. Single-diode equivalent circuit of one photovoltaic cell.

For the two effective cell groups, the current-voltage relations are written as

$$I_a = I_{ph-a} - I_{s-a}\left(\exp\left(\frac{V_a+I_aR_{s-a}}{\eta_a V_{th-a}}\right)-1\right) - \frac{V_a+I_aR_{s-a}}{R_{sh-a}} \tag{3.13}$$

$$I_b = I_{ph-b} - I_{s-b}\left(\exp\left(\frac{V_b+I_bR_{s-b}}{\eta_b V_{th-b}}\right)-1\right) \tag{3.14}$$

and the module voltage is obtained from

$$V_m = V_a + V_b \tag{3.15}$$

To keep the identification problem tractable and preserve physical consistency, the following assumptions are imposed:

$$I_{s-c} = I_{s-a} = I_{s-b} \tag{3.16}$$

$$\eta_c = \eta_a = \eta_b \tag{3.17}$$

$$R_{s-c} = \frac{R_{s-a}}{N_{s-a}} = \frac{R_{s-b}}{N_{s-b}} \tag{3.18}$$

$$R_{sh-c} = \frac{R_{sh-a}}{N_{s-a}} \tag{3.19}$$

The resulting parameter vector has seven unknowns, including the number of cells operating in the lower-irradiance group, together with the photogenerated currents and the single-cell electrical parameters. This formulation is self-adaptive because the estimated number of affected cells and the current ratio between the two groups change according to the operating conditions, allowing the model to converge toward uniform behaviour when the mismatch is negligible and to increase its flexibility when the mismatch is present [10

The parameter-identification stage is formulated as an optimization problem based on fitting the D-SDM equations to the measured I-V curve. In order to evaluate the model consistently along the voltage axis, the implicit equations are reformulated so that the sub-block voltages can be calculated for a given module current. The voltage of group (a) is obtained through an explicit Lambert-W formulation, while the voltage of group (b) is obtained through a closed logarithmic expression [10]:

$$V_a = -I_m(R_{s-a} + R_{sh-a}) + R_{sh-a}\left(I_{ph-a} + I_{s-a}\right) - \eta_a V_{th-a} L_a \tag{3.20}$$

$$L_a = \mathcal{W}\left\{\frac{I_{s-a}R_{sh-a}\exp(\mathcal{S}_a)}{\eta_a V_{th-a}}\right\} \tag{3.21}$$

$$V_b = \eta_b V_{th-b} \ln\left(\frac{I_{ph-b} - I_m}{I_{s-b}} + 1\right) - I_m R_{s-b} \tag{3.22}$$

Using these expressions, the module current associated with each experimental voltage point is determined through a binary-search procedure that exploits the monotonicity of the I-V curve. The fitting error is not defined pointwise in a naive way. Instead, only the region of the curve where both groups operate at positive voltages is considered, and the discrepancy is quantified through the relative area between the measured and estimated curves [10]:

$$\mathcal{E} = \frac{\sum_{i=1}^{M-1}\left[\frac{|I_{exp}(i) - I_m(i)| + |I_{exp}(i+1) - I_m(i+1)|}{2}\right]\Delta V(i)}{\sum_{i=1}^{M-1}\left[\frac{I_{exp}(i) + I_{exp}(i+1)}{2}\right]\Delta V(i)} \tag{3.23}$$

This error definition is a key methodological element because it automatically restricts the fitting problem to the physically valid part of the curve and prioritizes consistency in the diagnostically relevant region.

The optimization itself is carried out using the Differential Evolution algorithm. In particular, the selected variant is DE/best/1/bin, which is well suited to the non-linear and non-separable nature of the identification problem. The control parameters are chosen as (F=0.8) and (Cr=0.9), and two variants are considered. In the first one, denoted D-SDM, the number of affected cells is treated as a real-valued variable. In the second one, denoted D-SDM-I, the same parameter is enforced as an integer by means of a repair stage after an initial unconstrained evolution. This methodology is important because it explains why the proposed approach remains robust while keeping the optimization computationally feasible for online diagnosis [10].

The benefit of the proposed model is first observed in the fitting stage. When the D-SDM and the uniform-assumption SDM are compared on the same measured characteristic, the proposed model follows the experimental behaviour more closely in the relevant region.

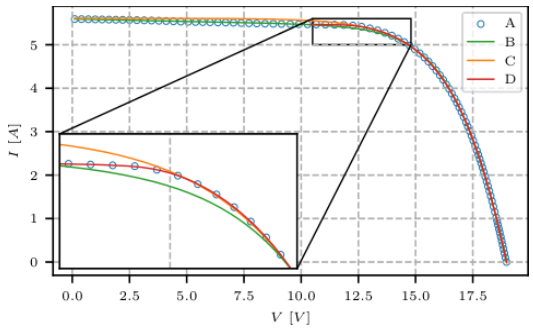

Fig. 3.19. Comparison of the uniform-assumption fitting and the proposed D-SDM fitting. The D-SDM better follows the measured current-voltage behaviour under mismatch conditions.

The fitting consistency of the proposed model for different mismatch cases is further illustrated below.

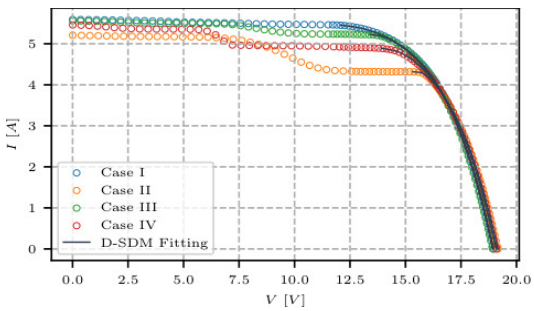

Fig. 3.20. Example of fitting results for experimental current-voltage curves under several mismatch patterns.

The best-fitting parameters obtained for the compared approaches are summarized below.

Table 4. Best fitting parameters of a single cell for D-SDM, D-SDM-I, and SDM.

Parameter	Case I			Case II			Case III			Case IV		
	D-SDM	D-SDM-I	SDM	D-SDM	D-SDM-I	SDM	D-SDM	D-SDM-I	SDM	D-SDM	D-SDM-I	SDM
$I_{ph\text{-}a}[A]$	5.44	5.48	5.61	4.31	4.31	4.39	5.22	5.22	5.35	4.88	4.87	4.98
$I_{s\text{-}c}[A]$	1.41×10^{-4}	1.56×10^{-4}	9.51×10^{-5}	8.88×10^{-5}	5.64×10^{-5}	2.69×10^{-9}	1.30×10^{-4}	1.25×10^{-4}	3.16×10^{-6}	5.84×10^{-5}	5.40×10^{-5}	1.59×10^{-7}
$\eta_c[-]$	1.96	1.98	1.89	1.93	1.85	1.00	1.92	1.92	1.43	1.84	1.83	1.22
$R_{s\text{-}c}[\Omega]$	0.0024	0.0023	0.0028	0.0025	0.0028	0.0068	0.0025	0.0026	0.0055	0.0029	0.0029	0.0069
$R_{sh\text{-}c}[\Omega]$	6.66	11.40	∞	27.81	30.34	∞	16.11	17.55	∞	6.53	7.06	∞
$I_{ph\text{-}b}[A]$	5.65	5.69	-	5.31	5.26	-	5.65	5.64	-	5.36	5.34	-
$N_{s\text{-}a}[-]$	1.00	4	-	1.00	1	-	1.00	1	-	1.18	1	-
Error $\mathcal{E}$	2.12×10^{-4}	2.21×10^{-4}	1.01×10^{-3}	2.96×10^{-4}	2.85×10^{-4}	1.36×10^{-2}	2.48×10^{-4}	2.48×10^{-4}	6.18×10^{-3}	1.88×10^{-4}	2.04×10^{-4}	5.99×10^{-3}

The previous table confirms two important points. First, both D-SDM-based variants achieve fitting errors one or two orders of magnitude lower than the SDM under mismatch conditions. Second, the parameters recovered by the proposed methods remain much more stable and physically interpretable than those obtained under the uniformity assumption.

This stability becomes clearer when the coefficient of variation of the identified parameters is compared across similar operating conditions for the different mismatch patterns.

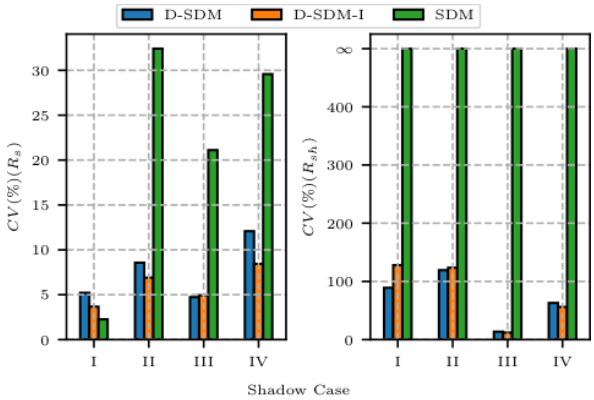

Fig. 3.21. Comparison of the coefficient of variation for R_s and Rsh

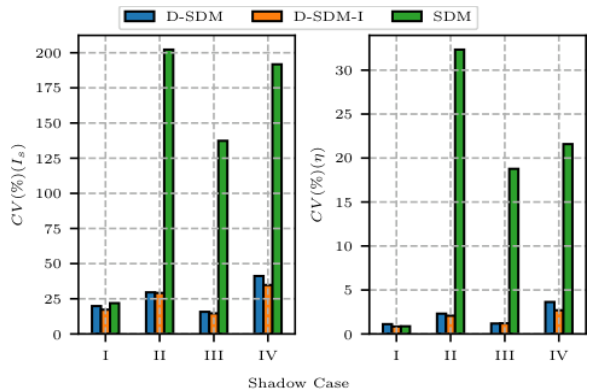

Fig. 3.22. Comparison of the coefficient of variation for I_s and eta

The coefficient-of-variation analysis shows that the proposed identification procedures provide substantially more stable parameter estimates across repeated measurements under comparable conditions. This is particularly important for diagnosis, because stable parameter trends are a prerequisite for distinguishing genuine degradation from estimation artifacts induced by mismatch.

The method was also validated through artificially generated current-voltage curves spanning a wide range of photovoltaic technologies and mismatch levels. In that study, the D-SDM parameters estimated from the synthetic curves were compared with the true parameters used for their generation, providing a direct numerical assessment of the identification accuracy [10].

Table 5. Used ranges for generating simulated curves.

Parameter	Lower Limit	Upper Limit
$N_s[-]$	16	120
$N_{s\text{-}a}[-]$	1	N_s
$I_{ph\text{-}b}[\mathrm{A}]$	2	12
$I_{ph\text{-}a}[\mathrm{A}]$	2	$I_{ph\text{-}b}$
$I_{s\text{-}c}[\mathrm{A}]$	10^{-12}	10^{-5}
$\eta_c[-]$	1	2
$R_{s\text{-}c}[\Omega]$	0.001	0.01
$R_{sh\text{-}c}[\Omega]$	10	50
$\nu[-]$	0.7	1.31
$T_c[K]$	273	343
$a[-]$	2×10^{-3}	15×10^{-3}
$m_{Bi}[-]$	2	6
$V_{br}[V]$	-40	-20

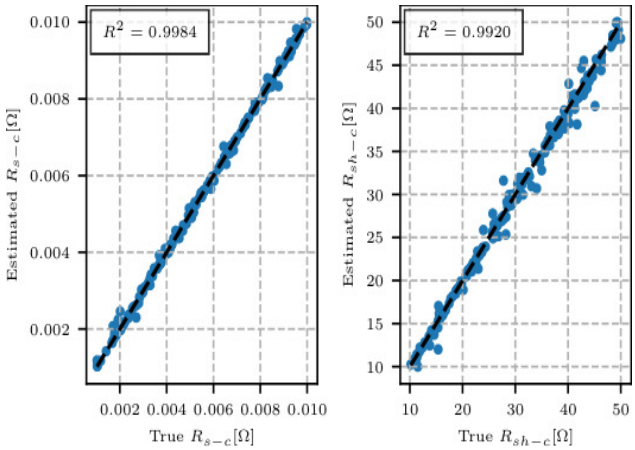

Fig. 3.23. True value versus estimation for Rs and Rsh

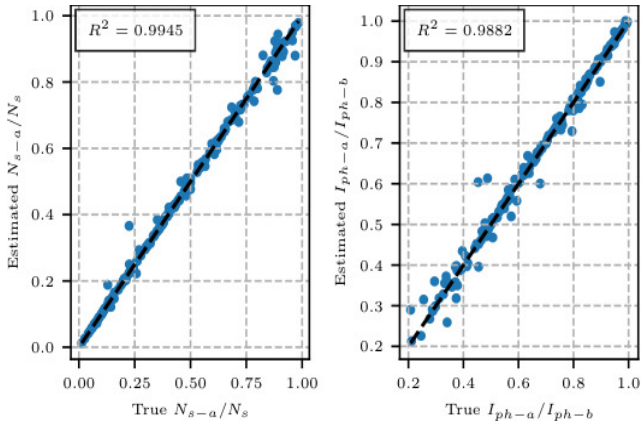

Fig. 3.24. True value versus estimation for the mismatch-related parameters

These simulated results confirm the accuracy of the proposed method to recover the true values of the model parameters.

Another key diagnostic result concerns the estimation of series resistance. Since series resistance is sensitive to degradation, a useful diagnosis-oriented model must produce values that remain stable with irradiance and are not dominated by mismatch artifacts [11]. The trends obtained with different approaches, including one approach based on Impedance Spectroscopy (CPE approach) [12], are shown below.

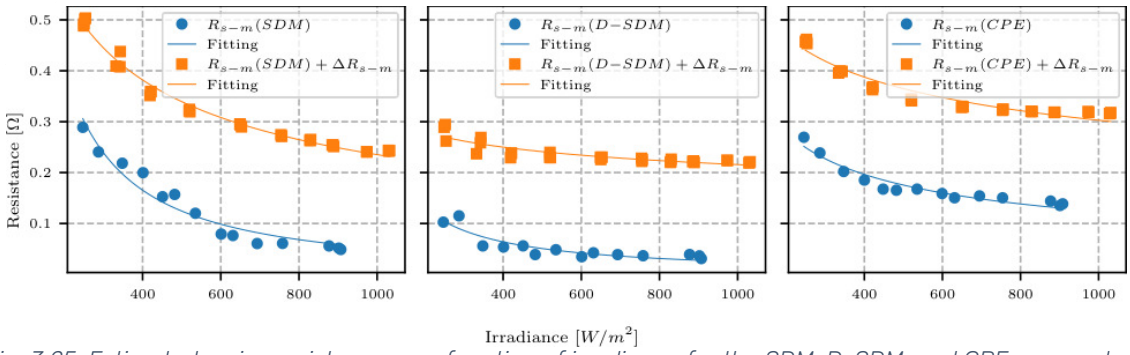

Fig. 3.25. Estimated series resistance as a function of irradiance for the SDM, D-SDM, and CPE approaches.

The D-SDM reports a stable behaviour across operating conditions.

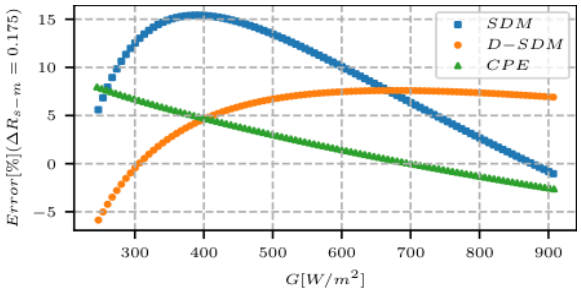

Fig. 3.26. Relative error in the estimation of series-resistance variation. The D-SDM provides a more balanced and stable trend than the uniform-assumption SDM.

Analysing three main operating conditions, low, median, and higher irradiance, we can compare the series resistance estimated by the models and the fitting errors.

Table 6. Operating Conditions for Each Selected Case.

Case	$T[K]$	$G[W/m^2]$
I	302.08	482.05
II	305.39	692.70
III	309.64	876.71

The comparative results are summarized below.

Table 7. Series Resistance and Fitting Error for Each Model.

Case	SDM		D-SDM		CPE	
	R_{s-m}	$\mathcal{E}$	R_{s-m}	$\mathcal{E}$	R_{s-m}	$\mathcal{E}$
I	0.157	0.0107	0.0394	0.0002	0.1654	0.0173
II	0.0607	0.0087	0.0364	0.0006	0.1542	0.0565
III	0.0560	0.0082	0.0395	0.0002	0.1441	0.0183

The D-SDM yields lower fitting errors and, more importantly, a much more stable series-resistance estimate across the considered irradiance range. This is the decisive advantage of the proposed method. The contribution is not only a better current-voltage fit, but the recovery of a parameter trend that remains interpretable for diagnosis under mismatching conditions [13].

3.3.5.Practical implementation of the integrated proposal

The third scientific outcome of IRP11 is the implementation of both intelligence layers in a common edge-computing environment and the experimental verification of their concurrent operation on a Raspberry Pi 4 platform running Home Assistant. This stage is not presented as an additional theoretical contribution, but as the validation that the two scientific methods can be transformed into software components suitable for practical smart-building deployment.

On the demand side, the aggregate power signal is acquired from the local monitoring environment (Shelly meter) [14], processed by the O2RE add-on, and converted into virtual entities associated with appliance-level power, base load, and unknown-load activity. The corresponding deployment architecture is shown below.

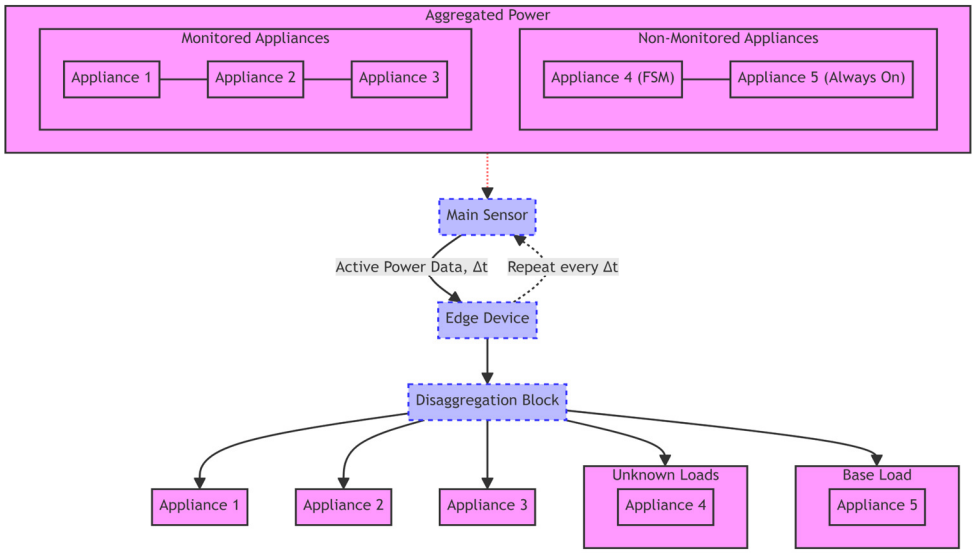

Fig. 3.27. Deployment architecture of the demand-side intelligence prototype, from aggregate active power to appliance-level outputs.

The practical configuration of the add-on is performed through a dedicated interface in which the input power sensor and the appliance models are defined.

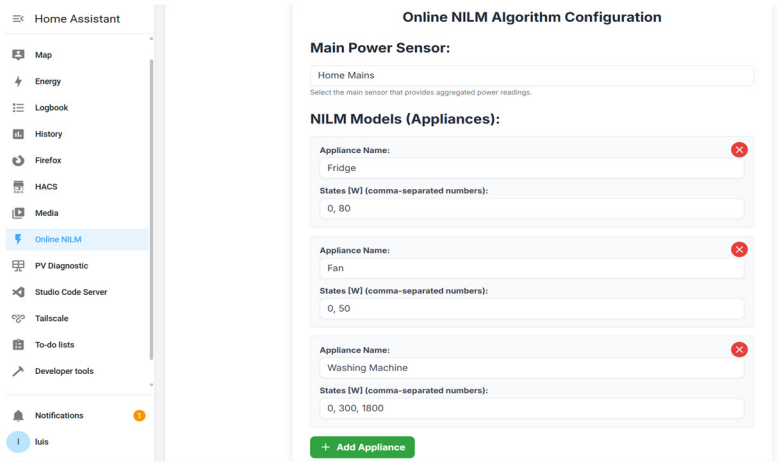

Fig. 3.28. Configuration interface of the demand-side add-on inside the unified platform.

The runtime results obtained for the demand-side routine during deployment are summarized below.

Table 8. Runtime summary of the O2RE demand-side add-on during deployment.

Statistic	Time (seconds)
Mean (All)	0.004
Mean (>0.05s)	0.071
Maximum (>0.05s)	0.132

These values confirm that the demand-side algorithm can operate in real time on shared embedded hardware, which is a necessary condition for its integration with the other services of an energy management platform.

On the supply side, the diagnosis workflow receives current-voltage data from the inverter, executes the parameter-identification stage on the edge device, and publishes the resulting photovoltaic entities to the same software platform. The deployment architecture is reported below.

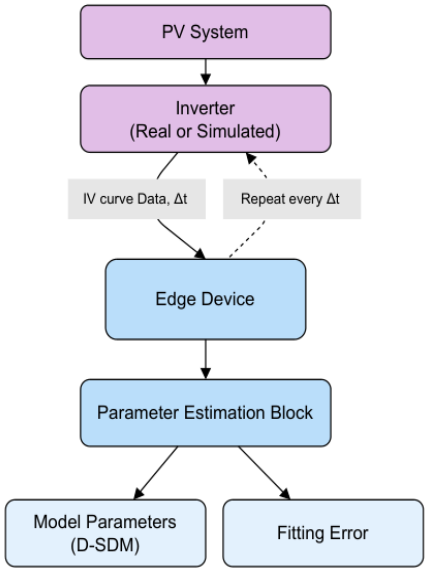

Fig. 3.29. Deployment architecture of the photovoltaic diagnosis add-on inside the edge platform.

The corresponding visualization of the diagnosis results is shown below.

Fig. 3.30. Visualization of photovoltaic parameter-estimation results within the unified platform.

The runtime percentiles of the photovoltaic routine are summarized below.

Table 9. Runtime percentiles and implied safe launch rates.

Percentile	Runtime (s)	Max launches h^{-1}
25^{th} (Q_1)	128.3	28.0
50^{th} (Median)	234.3	15.4
75^{th} (Q_3)	390.4	9.2
90^{th}	523.5	6.9
95^{th}	566.4	6.4

These results show that the photovoltaic diagnosis routine remains schedulable within realistic monitoring intervals on the embedded device.

The final verification step consisted of running both add-ons concurrently in the same Home Assistant environment. The integrated view is illustrated below.

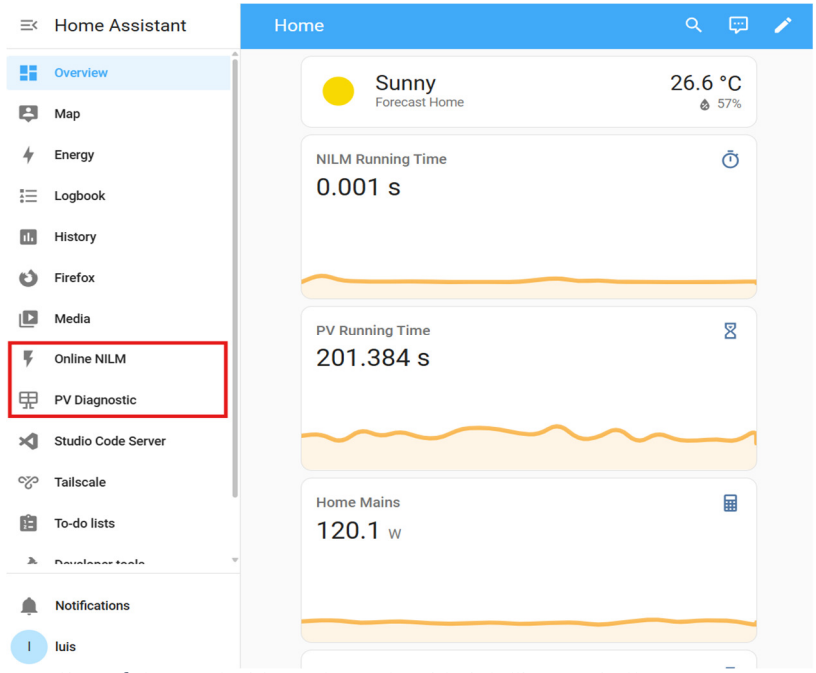

Fig. 3.31. Concurrent operation of demand-side and supply-side intelligence in the same Home Assistant environment.

The concurrent operation demonstrates that the two methods are compatible at the software, data, and runtime levels. Appliance-level demand information and photovoltaic diagnosis indicators can be generated locally, exposed as platform entities, and used within the same edge environment without resorting to cloud computation. In practical terms, this implementation verifies the feasibility of a complete monitoring layer for smart-building energy management, combining demand-side disaggregation and supply-side diagnosis on a single embedded device [14].

3.3.6.Contribution to the WP objectives

IRP11 contributes to the objectives of WP4 by delivering scientifically validated methods and an embedded implementation that reinforce the observability, interpretability, and future controllability of smart-building energy management systems.

First, in line with WP4 objective (i), IRP11 identifies and demonstrates new ways of using electrical energy information for energy storage and consumption strategies through advanced monitoring and exogenous information. Rather than relying solely on aggregate power measurements, IRP11 extracts appliance-level demand, base-load indicators, unknown-load activity, photovoltaic mismatch information, and degradation-sensitive parameters. These outputs significantly enrich the informational basis of the energy management system, enabling future optimization and control decisions to be more informed, targeted, and physically meaningful [15].

Second, in direct relation to WP4 objective (ii), IRP11 supports energy consumption reduction through the use of emerging digital technologies. The proposed demand-side and supply-side methods are specifically designed for edge deployment, execution on low-cost hardware, and local processing. This makes the solution compatible with smart-metering environments and embedded building technologies, while avoiding dependence on costly sensing infrastructures or cloud-based computation [15].

Third, with respect to WP4 objective (iii), IRP11 analyses and demonstrates the benefits of cooperation between power converters and ICT within Energy Management Systems. On the demand side, appliance power-state transitions are converted into digital entities that can be detected, classified, and processed in real time. On the supply side, current-voltage measurements from the photovoltaic generator are transformed into compact model parameters associated with mismatch and degradation phenomena. The resulting platform shows how converter-level electrical behaviour and ICT-based intelligence can be integrated coherently within a common software framework [15].

Fourth, in accordance with WP4 objective (iv), IRP11 contributes to the identification of energy-related behavioural change requirements by exposing interpretable and user-relevant variables rather than only raw electrical measurements. Appliance-level indicators help reveal energy-intensive uses and persistent base-load consumption, while photovoltaic parameter trends can improve user awareness of system health and local generation performance. Such information is well suited for dashboards, alerts, and future decision-support tools aimed at strengthening customer engagement in energy applications [15].

Finally, beyond its direct contributions to the four WP4 objectives, IRP11 also prepares the ground for future EMS optimization functions. Although its present focus is on diagnosis and monitoring rather than direct control, it establishes the necessary preconditions for optimization by providing structured observability on both sides of the meter. Appliance-level demand intelligence can subsequently support scheduling, load shifting, and flexibility assessment, while photovoltaic parameter intelligence can support performance-aware control and maintenance planning. In this way, the integrated edge platform forms a concrete technological bridge between scientific diagnostic methods and future building-level optimization strategies within WP4 [15].

3.3.7. Scientific achievements

Experimental prototypes

#	Name	Description	Status (designed, assembled, tested)	Photo
1	O2RE demand-side add-on	Real-time load-disaggregation software generating appliance-level, base-load, and unknown-load entities from aggregate active power	Developed and validated	  
2	D-SDM photovoltaic add-on	PV component generating diagnosis-oriented PV parameters and fitting-quality indicators from current-voltage data	Developed and validated	

3	Unified edge platform	Home Assistant-based platform integrating both previous components in a shared Raspberry Pi 4 environment	Developed and validated	 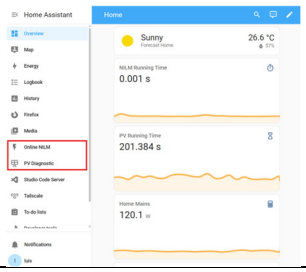

Publication

#	Title, incl. citation information	Type (Conference, journal, book chapter)	Status (Submitted, accepted, published)	DOI
1	Garcia-Marrero, Monmasson, Petrone, "Online real-time robust framework for non-intrusive load monitoring in constrained edge devices"	Journal	Published	10.1016/j.apenergy.2024.124814
2	Garcia-Marrero, Pavon-Vargas, Bastidas-Rodriguez, Monmasson, Petrone, "Self-adaptive single-diode model parameter identification under small mismatching conditions"	Journal	Published	10.1016/j.renene.2025.122735
3	Garcia-Marrero, Petrone, Monmasson, "Transfer capabilities of Seq2Seq and Seq2Point CNN architectures in Non-intrusive Load Monitoring with unseen appliances."	Journal	Published	10.1016/j.matcom.2025.05.021
4	Piliougine, Garcia-Marrero, Lappalainen, Spagnuolo, "Influence of the temperature on the intrinsic parameters of thin-film photovoltaic modules"	Journal	Published	10.1016/j.renene.2024.122068
5	Pavon-Vargas, Garcia-Marrero, Bastidas-Rodriguez, Guejia-Burbano,	Journal	Published	10.1109/TIA.2025.3561708

	Petrone, "Experimental Assessment of Partial Shading Detection in PV Panels Using Impedance Spectroscopy"			
6	Pavon-Vargas, Garcia-Marrero, Petrone, "Dynamic Photovoltaic Modeling for Circuit-Emphasis Simulation"	Journal	Submitted	N/A
7	Garcia Marrero, Guejia-Burbano, Petrone, Piliougine, Monmasson, "Identification of static and dynamic parameters of PV models through multi-objective optimization"	Conference	Published	10.1109/CPE-POWERENG58103.2023.10227400
8	Garcia-Marrero, Piliougine, Petrone, De Riso, Guerriero, Monmasson, "Challenges in photovoltaic parameter identification under mismatching conditions"	Conference	Published	10.1109/ICCEP57914.2023.10247445
9	Garcia-Marrero, Petrone, Monmasson, "Detection of Series Resistance Degradation in PV Modules Using Measured Current-Voltage and Frequency-Domain Impedance"	Conference	Published	10.1109/ICCEP65222.2025.11143628
10	Pavon-Vargas, Garcia-Marrero, Petrone, Curcio, "An enhanced single-diode model of photovoltaic panels for SPICE simulations"	Conference	Accepted	Springer Lecture Notes in Electrical Engineering
11	Garcia-Marrero, Pavon-Vargas, Petrone, Monmasson, "Advancements in Photovoltaic Research: Electro-Impedance Spectroscopy for PV Cell Characterization"	Conference	Published	10.1109/SPEEDAM61530.2024.10609231

12	De Riso, Matacena, Guerriero, Daliento, Garcia-Marrero, Petrone, "Dynamic Modeling of Si-based Photovoltaic Modules using Impedance Spectroscopy Technique"	Conference	Published	10.1109/ICCEP57914.2023.10247369
13	Pavon-Vargas, Guejia-Burbano, Garcia-Marrero, Petrone, "Impedance Spectroscopy for partial shading detection on series-connected PV panels"	Conference	Published	10.1109/SPEEDAM61530.2024.10609152

4. Conclusions

Work Package 4 of the SMARTGYSUM project has successfully fulfilled its primary objectives, delivering substantial scientific and technological advancements in the domain of end-user energy systems and prosumer applications. Over the course of the project, the coordinated efforts across the three Individual Research Projects have produced innovative strategies for managing electric energy and storage, optimized the cooperation between power electronics and Information and Communication Technologies, and established robust methodologies for monitoring and controlling residential microgrids. A unifying success of this work package has been the practical shift of complex computational tasks—such as load forecasting, energy management optimization, and system diagnostics—away from cloud-dependent architectures and onto localized, low-cost edge computing platforms.

The research outcomes have demonstrated tangible progress on multiple fronts. Through Task 4.1, a highly accurate, bottom-up residential load generation and optimization framework was developed and successfully embedded into practical smart home ecosystems, proving the viability of degradation-aware energy management. Meanwhile, Task 4.2 significantly advanced the operational stability and economic efficiency of residential microgrids by deploying advanced, price-based control strategies and centralized communication protocols, rigorously validated through Controller Hardware in the Loop experimental setups. Finally, Task 4.3 provided critical breakthroughs in both demand-side and supply-side intelligence for smart buildings, introducing a highly resilient Non-Intrusive Load Monitoring framework and an adaptive photovoltaic diagnostic model capable of operating reliably under mismatched conditions.

Beyond the technical prototypes and validated software frameworks, Work Package 4 has generated a strong academic footprint, yielding numerous peer-reviewed publications and contributing directly to the successful defense of a jointly awarded double Ph.D. degree. Ultimately, the methodologies and deployable embedded technologies developed within this work package equip future energy systems with the localized intelligence, fault tolerance, and interpretability required to empower prosumers. By effectively bridging the gap between advanced theoretical modeling and practical edge-level implementation, WP4 has laid a critical foundation for the modernization, resilience, and sustainability of smart buildings and residential microgrids across Europe.

5. References

[1] T. Jalakas, A. Chub, I. Roasto, D. Vinnikov, and J. Kurnitski, "Design and development of solid state circuit breaker with residual current protection for residential prosumer DC microgrids," PEAS, vol. 74, no. 2S, pp. 281–290, May 2025, doi: 10.3176/proc.2025.2S.02.

[2] V. Khare and P. Chaturvedi, "Design, control, reliability, economic and energy management of microgrid: A review," e-Prime - Advances in Electrical Engineering, Electronics and Energy, vol. 5, p. 100239, Sep. 2023, doi: 10.1016/j.prime.2023.100239.

[3] J. M. Guerrero, J. C. Vasquez, J. Matas, L. G. de Vicuna, and M. Castilla, "Hierarchical Control of Droop-Controlled AC and DC Microgrids—A General Approach Toward Standardization," IEEE Transactions on Industrial Electronics, vol. 58, no. 1, pp. 158–172, Jan. 2011, doi: 10.1109/TIE.2010.2066534.

[4] "Low-code programming for event-driven applications: Node-RED." Accessed: Mar. 01, 2026. [Online]. Available: https://nodered.org/

[5] S. Hasan, A. Blinov, A. Chub, and D. Vinnikov, "Solar PV Generation and Consumption Dataset of an Estonian Residential Dwelling," Sci Data, vol. 12, no. 1, p. 481, Mar. 2025, doi: 10.1038/s41597-025-04747-w.

[6] A. Bakeer, A. Chub, Y. Shen, and A. Sangwongwanich, "Reliability analysis of battery energy storage system for various stationary applications," Journal of Energy Storage, vol. 50, p. 104217, Jun. 2022, doi: 10.1016/j.est.2022.104217.

[7] L.E. Garcia-Marrero, G. Petrone, and E. Monmasson, "Transfer capabilities of Seq2Seq and Seq2Point CNN architectures in Non-intrusive Load Monitoring with unseen appliances," Mathematics and Computers in Simulation, vol. 239, Jan. 2026, pp. 211–222. DOI: 10.1016/j.matcom.2025.05.021

[8] L. E. Garcia-Marrero, E. Monmasson, and G. Petrone, "Online real-time robust framework for non-intrusive load monitoring in constrained edge devices," Applied Energy, vol. 378, 2025, 124814. DOI: 10.1016/j.apenergy.2024.124814.

[9] L. E. Garcia-Marrero, M. Piliougine, G. Petrone, M. De Riso, P. Guerriero, and E. Monmasson, "Challenges in photovoltaic parameter identification under mismatching conditions," 2023 International Conference on Clean Electrical Power, 2023. DOI: 10.1109/ICCEP57914.2023.10247445.

[10] L. E. Garcia-Marrero, C. I. Pavon-Vargas, J. D. Bastidas-Rodriguez, E. Monmasson, and G. Petrone, "Self-adaptive single-diode model parameter identification under small mismatching conditions," Renewable Energy, vol. 245, 2025, 122735. DOI: 10.1016/j.renene.2025.122735.
[11] L.E. Garcia-Marrero, G. Petrone, and E. Monmasson, "Detection of Series Resistance Degradation in PV Modules Using Measured Current-Voltage and Frequency-Domain Impedance," 2025 ICCEP, Jun. 2025, pp. 250–255. DOI: 10.1109/ICCEP65222.2025.11143628
[12] L. E. Garcia-Marrero, R. A. Guejia-Burbano, G. Petrone, M. Piliougine, and E. Monmasson, "Identification of static and dynamic parameters of PV models through multi-objective optimization," 2023 IEEE 17th International Conference on Compatibility, Power Electronics and Power Engineering, 2023. DOI: 10.1109/CPE-POWERENG58103.2023.10227400.
[13] Home Assistant, open-source home automation platform, https://www.home-assistant.io/.
[14] Shelly EM with 50 A clamp, manufacturer documentation.
[15] L. E. Garcia-Marrero, "On-line diagnosis and optimization of energy management systems for smart buildings," Ph.D. dissertation, CY Cergy Paris Univ., Cergy, France, jointly supervised with Univ. degli Studi di Salerno, Salerno, Italy, 2025. [Online]. Available: https://theses.fr/2025CYUN1413